Does additive manufacturing cause intergranular oxidation attack in high-temperature alloys? Case study of Ni-base alloy IN625

Citation for the original published paper (version of record):
Chyrkin, A., Roth, J., Naumenko, D. et al (2026). Does additive manufacturing cause intergranular oxidation attack in high-temperature alloys?
Case study of Ni-base alloy IN625. Corrosion Science, 260.
http://dx.doi.org/10.1016/j.corsci.2025.113588

Corrosion Science 260 (2026) 113588

Contents lists available at ScienceDirect

Corrosion Science

journal homepage: www.elsevier.com/locate/corsci

Does additive manufacturing cause intergranular oxidation attack in high-temperature alloys? Case study of Ni-base alloy IN625☆

A. Chyrkin [a,*], J.-P. Roth [b], D. Naumenko [c], K. Jahns [b]

[a] Chalmers University of Technology, Department of Chemistry and Chemical Engineering, Kemivägen 10, Gothenburg 412 58, Sweden
[b] University of Applied Sciences Osnabrück, Faculty of Engineering and Computer Science, Osnabrück 49076, Germany
[c] Forschungszentrum Jülich GmbH, Institute for Energy Materials and Devices (IMD-1), Leo-Brandt-Straße, Jülich 524 25, Germany

ARTICLE INFO

Keywords:
Additive manufacturing
Ni-base alloy
IN625
High-temperature oxidation
Porosity

ABSTRACT

High-temperature oxidation of additively manufactured (AM) Ni-base alloy IN625 has been studied in air and Ar-4 %H_2-2 %H_2O for up to 1000 h at 900 and 1000 °C. AM was produced from the same conventionally manufactured (CM) reference alloy batch to retain the chemical composition and minimize batch-to-batch variation. The AM alloy developed subsurface porosity during oxidation, but the intergranular voids remained closed and unoxidized because of good adhesion of the Cr_2O_3 scale to the metal. Contrary to many literature studies, AM had no effect on either the oxide growth kinetics or the oxide adherence. The chemical composition of the currently studied AM alloy close to the CM, especially the minor elements e.g. Al, Mn, Si and Ti, is believed to be the key factor preventing oxide decohesion and intergranular oxidation attack.

1. Introduction

Ni-base superalloys are state-of-the-art structural materials for high-temperature applications in petrochemical industries, heat processing, aero-engine technology, power generation, etc. Most of these applications require high creep strength as well as high oxidation and/or corrosion resistance to operate in harsh corrosive environments at elevated temperatures [1]. Alloy Inconel 625 [2] is a popular Cr_2O_3--scale forming Ni-base alloy, which finds applications in high-pressure steam lining, nuclear power generation, marine and aerospace industries.

Additive manufacturing (AM) of alloys has recently developed into a separate dynamic branch offering a high degree of flexibility in design and complexity of geometries as well as much lower material waste compared to conventional machining routes [3–6]. As AM process involves fast cooling rates and directional solidification resulting in highly inhomogeneous and anisotropic alloy microstructures [7], the key properties of AM-Ni-base alloys such as creep/fatigue strength and oxidation/corrosion resistance might be compromised by AM.

Recent studies of Ni-base alloys produced using powder bed fusion - laser beam (PBF-LB/M) process such as alloy IN625 [8,9] and alloy IN718 [10–12] demonstrate that creep rates of the optimized AM alloys can be achieved on the level of the wrought, conventionally manufactured (CM) counterparts. At the same time, the oxidation resistance of theses AM alloys remains systematically inferior to that of CM. Over the past decade, oxidation behavior of AM high-temperature alloys [13–18], especially alloy IN625 [19–31] and alloy IN718 [32–37], has been addressed in numerous studies resulting in a consensus on two main observations: i) there is no oxidation rate anisotropy, ii) AM alloys are likely to suffer from intergranular oxidation attack (IGOA), i.e., internal oxidation of Cr in an alloy designed to grow external Cr_2O_3 scales, and thus have higher oxygen uptakes.

IGOA needs to be differentiated from a classical intergranular oxidation (IGO) occurring in high-temperature alloys such as precipitation of Al_2O_3 along the alloy grain boundaries (GBs) underneath an external Cr_2O_3 scale as demonstrated in e.g. CM IN625 [38]. IGOA in AM alloy IN625 [19–26,28,30,31] and IN718 [33,34,37] has a characteristic and reproducible oxidation morphology, i.e., a buckled Cr_2O_3 scale (at very early oxidation stages) or a compact oxide ridge (at longer oxidation times) is accompanied by elongated voids underneath the ridge. After longer exposures, these voids are filled with Cr_2O_3. This ridge-void (RV) morphology was repeatedly encountered after various annealing

☆ All persons who meet authorship criteria are listed as authors, and all authors certify that they have participated sufficiently in the work to take public responsibility for the content, including participation in the concept, design, analysis, writing, or revision of the manuscript. Furthermore, each author certifies that this material or similar material has not been and will not be submitted to or published in any other publication before its appearance in *Corrosion Science*.

* Corresponding author.
E-mail address: chyrkin@chalmers.se (A. Chyrkin).

https://doi.org/10.1016/j.corsci.2025.113588
Received 13 September 2025; Received in revised form 27 November 2025; Accepted 30 December 2025
Available online 31 December 2025

regimes and hot-rolling of AM alloy and was hypothesized by Chyrkin et al. [22,23] to originate from the minor differences in chemical composition of AM and CM, i.e., lower Si content in AM alloy IN625. Moderate alloying with Si is well-known to improve oxidation resistance of chromia-forming alloys [39–42]. Even though the experiments with model alloys in [23] demonstrated a beneficial effect of Si suppressing IGOA, it does not necessarily prove the beneficial effect of Si in the case of AM alloy IN625 in [22,23], given the complexity of its microstructure. To unequivocally verify the claimed effect of Si and possibly other minor alloying elements, a batch of AM alloy IN625 with the identical chemical composition of CM would be required. In all afore-mentioned studies comparing oxidation behavior of AM and CM, the alloy specimens come from different batches and, hence, differ in chemical composition. The latter raises an important question: to what extent do the differences in oxidation behavior between AM and CM alloys reported in [13–37] originate from batch-to batch variations [43] or are they rather due to additive manufacturing and the resulting AM microstructures?

In the present paper, AM alloy IN625 was manufactured from the same CM batch previously studied in [38]. It should be also borne in mind that AM is known to affect to some extent the chemical composition of the alloy as alloy atomization introduces the excessive oxygen and nitrogen into the alloy powder. Furthermore, the minor deoxidizers such as Al, Mn, Si and Ti are likely to react with oxygen or nitrogen during atomization and thus may be lost in the AM process. However, comparing the AM alloy with its original CM precursor is the best available option to shed the light on the effect of alloy chemistry. In summary, the goal of the present study is to minimize the batch-to-batch variation and focus on the effects of oxidation behavior related solely to the AM process.

2. Experimental procedure

2.1. Materials

The conventionally manufactured (CM) alloy IN625 was a forged bar supplied by Huntington Alloy Corp. This CM alloy batch was studied in [38]. The same batch was used for production of powder for PBF-LB/M. IN625 powder was produced by gas atomization using an Indutherm BluePower AU3000 atomizer in close-coupled mode. The starting material was inductively melted at 1650 °C in a ceramic crucible, held for 30 min, and then introduced through an outlet valve into the atomizer nozzle, where it was atomized under argon at 12 bar with a gas flow of 360 m^3 /h. During gas atomization, the cooling rate ranged from 10^5 to 10^8 K/s. The resulting powder was first sieved through a 63 μm mesh to remove coarse particles and then air-classified to eliminate fine fractions below 10 μm. For additive manufacturing, the powder was processed by laser powder bed fusion (PBF-LB/M) using an EOS M290 customized machine equipped with a 500 W 532 nm laser. Hereby, 20 μm layers of powder with particle sizes of approximately 10–60 μm were spread on a build platform and locally melted. After solidification, the platform was lowered by one layer thickness and new powder was applied. The quality and density of the melt tracks are governed by laser power, scan speed, layer height, and hatching distance. In this work, a laser power of 95 W, a scan speed of 1380 mm/s, a layer thickness of 0.020 mm and a hatching distance of 0.05 mm were employed, resulting in a volume energy density of 61.6 J/mm^3 . The additively manufactured test samples (AM) exhibited a relative optical density of 99.5.

The differences in chemical composition between CM and AM were negligible. The chemical compositions of AM and CM alloy IN625 obtained by Inductively coupled plasma – Optical emission spectrometry (ICP-OES) and infrared (IR) combustion analysis are listed in (Table 1).

The alloy coupons of CM IN625 were machined from the forged bar to 12 × 12 × 2 mm^3 dimensions. The alloy coupons of AM IN625 were machined to 10 × 10 × 2 mm^3. The surfaces were ground with SiC papers to 1200 grit. Several exposures were carried out with mirror polished coupons, 1 μm as e.g. in [22,23], and did not reveal any measurable differences in oxidation kinetics between the ground and polished AM and CM alloy specimens. The 1200 grit surface finish was selected for the present study to ensure a comparability with the data for CM in [38].

2.2. Thermobalance exposures

The *in-situ* oxidation kinetics measurements were isothermally performed with a SETARAM thermobalance in flowing synthetic air and Ar-4 %H_2-2 %H_2O for up to 72 h at 900 and 1000 °C. The heating rate was 90 K min^{-1}. The cooling rate was 10 K min^{-1}.

2.3. Long-term air exposures

The CM and AM specimens were discontinuously exposed in air and Ar-4 %H_2-2 %H_2O for up to 1000 h at 900 and 1000 °C, recapitulating the test program in [38]. Exposures were performed in a horizontal tube furnace (⌀ 44 mm). The temperature calibration was performed by an external Pt/Rh-thermocouple to establish a 4 cm wide zone of stable temperature in the furnace.

The air exposures were carried out in quartz tubes in stagnant lab air. The specimens were degreased in ethanol and acetone prior to exposure and directly introduced into the hot zone of the tube furnace. After a dwell time, the specimens were removed from the hot zone of the furnace and cooled down in air and re-introduced into the furnace after weighing.

The exposures in Ar-4 %H_2-2 %H_2O gas mixtures were carried out in an alumina tube in a horizontal furnace. The Ar-4 %H_2 gas mixture supplied by Linde Gas was bubbled through a humidifier kept at 17.5 °C. The alloy specimens were introduced into a cold furnace, flushed with the dry Ar-4 %H_2 gas for 1 h and heated at 10 K min^{-1} to reach the exposure temperature. The humidification was turned on once the furnace reached the target temperature. The cooling rate was 10 K min^{-1} as well. The gas flow rate was set at 200 ml min^{-1}.

The mass gain curves were obtained by gravimetric measurements prior to and after the exposures using Mettler Toledo XP6 microbalance with a 1 μg resolution.

Table 1
Chemical composition of as-forged CM and AM alloy IN625 in wt% in form of atomized powder and as-printed specimen determined by ICP-OES and IR combustion analysis. The alloying elements are grouped according by their metallurgical functionality and oxidation behavior.

Base		δ-phase		neutral		oxide scale		internal oxides		interstitials		
Ni [wt%]	Cr [wt%]	Mo [wt%]	Nb [wt%]	Fe [wt%]	Cu [wt%]	Mn [wt%]	Ti [wt%]	Al [wt%]	Si [wt%]	C [wt%]	O [wt%]	N [wt%]
CM IN 625												
Bal.	21.5	9.1	3.5	3.61	0.19	0.11	0.33	0.32	0.27	0.02	0.001	0.013
IN 625 powder												
Bal.	21.3	9.0	3.26	3.57	0.30	0.09	0.33	0.30	0.35	0.04	0.013	0.041
AM fabricated IN 625												
Bal.	21.6	9.1	3.23	3.60	0.31	0.10	0.33	0.30	0.23	0.06	0.019	0.044

2.4. Microstructural characterization

Electron backscatter diffraction (EBSD) maps were obtained on as-received materials using a Zeiss Ultra 55 field emission gun (FEG) scanning electron microscope (SEM) equipped with an HKL Channel 5 EBSD detector. An FEI Quanta 200 SEM equipped with an Oxford X-max 80 energy dispersive X-ray spectrometer (EDX) was employed for pre- and post-exposure analyses. Aztec software was used to evaluate the EDX data. Cross-sections of the as-printed and exposed alloy samples were prepared by mechanical polishing. The exposed specimens were gold sputtered and electroplated with nickel prior to mounting to ensure the integrity of the oxidation products. The specimens were hot mounted using the conductive mounting resin PolyFast (Struers, Denmark). The mounted specimens were ground with SiC papers to 4000 grit and further polished with diamond pastes to 0.25 μm. The final preparation step was polishing with an alkali solution of colloidal silica OP-S (Struers, Denmark).

3. Results

3.1. Material microstructure

SEM BSE images in Fig. 1 demonstrate the microstructure of as-printed AM (a,b – transversal cut, c,d – longitudinal cut) and CM (e,f) alloy IN625. The EBSD inverse pole figures (IPF) maps in Fig. 2 show a common microstructure of AM alloy IN625, previously reported in [22, 44], consisting of vertical melt pools 30–40 μm in width aligned along the build axis Z. The melt pools contain submicron dendritic cells (Fig. 1**b,d**). The forged CM alloy IN625 contains equiaxed grains with the average grain size of 12 μm.

3.2. Thermogravimetry

Fig. 3 shows *in-situ* TG-curves for CM and AM alloy IN625 measured in thermobalance during exposures in synthetic air and Ar-4 %H_2-2 % H_2O for 72 h at 900 and 1000 °C. Remarkably, the curves for CM and AM

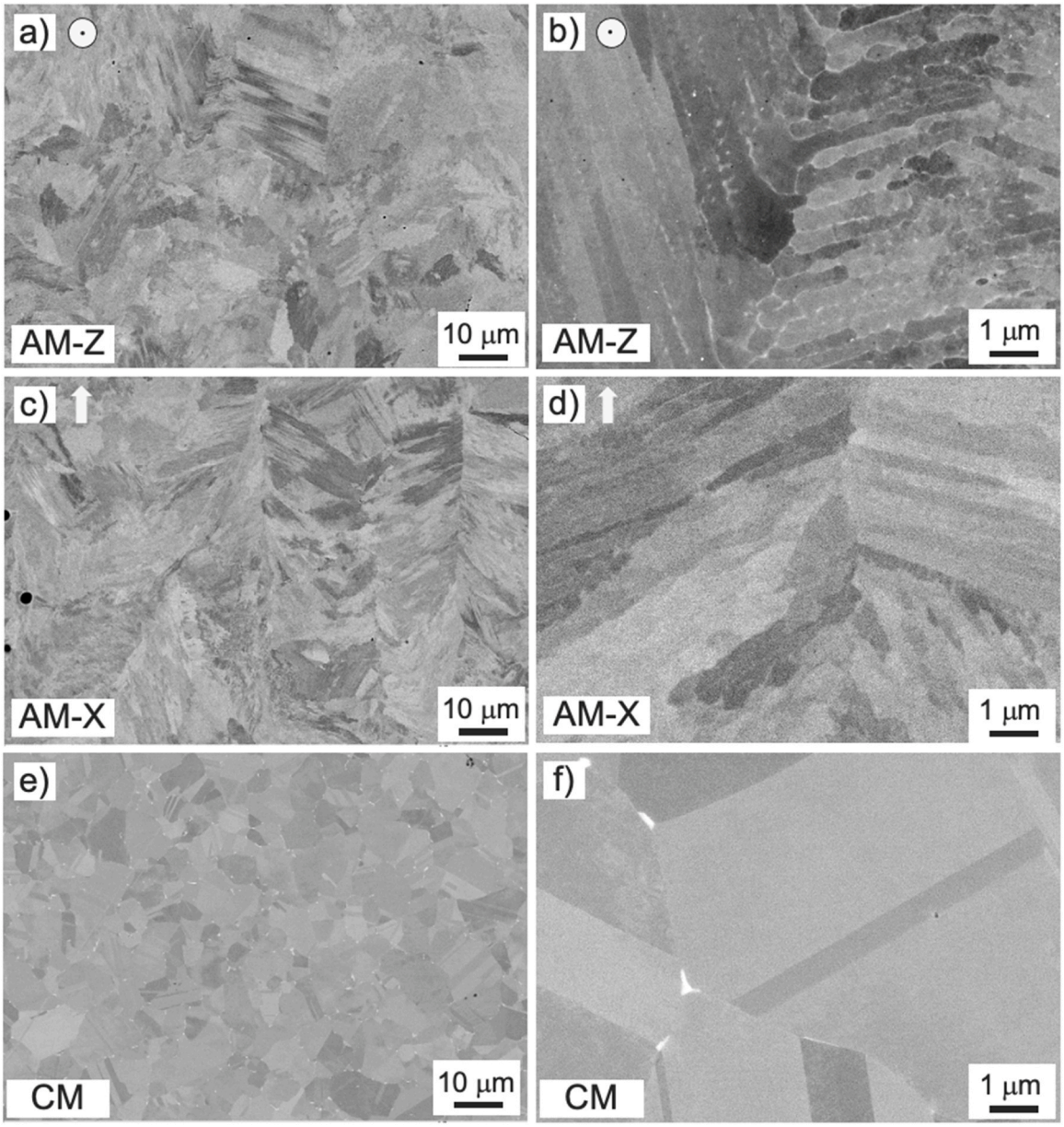

Fig. 1. SEM BSE images of as-received AM (a-d) and CM (e,f) alloy IN625. AM alloy was sectioned transversally (AM-Z in fig. a,b indicated by circles) and longitudinally (AM-X in fig. c,d indicated by arrows) with respect to the build direction.

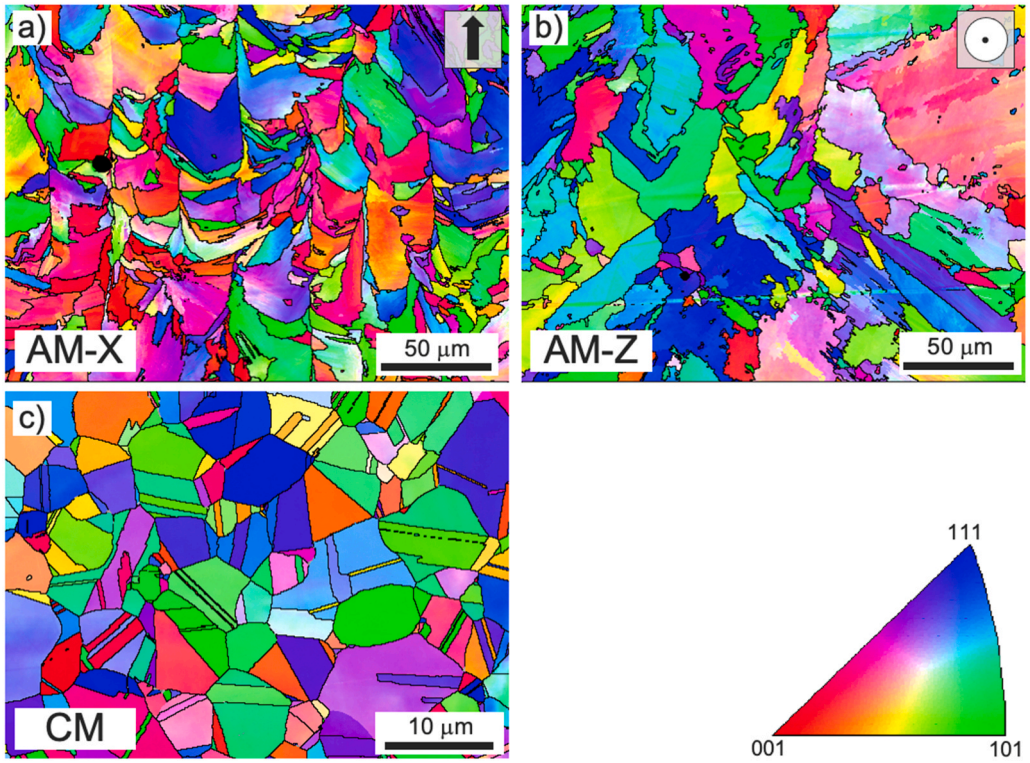

Fig. 2. EBSD maps for as-printed AM (a,b) and CM (c) alloy IN625. AM alloy was sectioned longitudinally (AM-X in fig. a, build direction indicated by arrow) and transversally (AM-Z in fig. b, build direction indicated by circle).

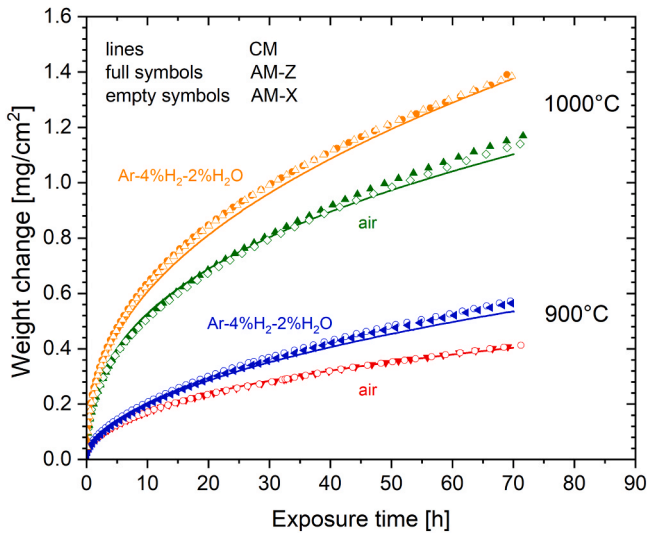

Fig. 3. Weight change curves recorded in-situ for AM (symbols) and CM (lines) alloy IN625. Specimens were exposed in synthetic air (in red and green) and Ar-4 %H_2-2 %H_2O (in blue and orange) for 72 h at 900 °C and 1000 °C. Full symbols denote the longitudinal cut AM-X, empty symbols denote the transversal cut AM-Z.

are virtually identical for all four conditions, i.e., two temperatures and two different atmospheres. At both 900 and 1000 °C, the oxidation rate is slightly higher in Ar-4 %H_2-2 %H_2O compared to air.

These trends were fully reproduced in discontinuous long-term furnace exposures for up to 1000 h (Fig. 4). The oxidation rates agree well with previously reported data for this batch of IN625 [38]. The oxidation kinetics is parabolic (Fig. 3). At 1000 °C, both AM and CM are prone to weight loss due to oxide spallation after 300 h in air while in Ar-4 %H_2-2 %H_2O the oxygen uptake is continuous, i.e., no oxide spallation occurs even after 1000 h of discontinuous exposures at 1000 °C.

3.3. Oxide scale morphologies

Fig. 5 illustrates BSE images of cross-sectioned CM and AM alloy IN625 specimens exposed in air for 24 h (a, b, c) and 1000 h (d, e, f) at 900 °C. Microscopy for air exposures at 1000 °C is not demonstrated due to severe oxide spallation as can be seen from the mass changes in Fig. 4. The CM specimens reproduced the oxidation morphology reported for this alloy batch in [38], i.e., (i) an external Cr_2O_3 scale is accompanied by internal precipitation of Al_2O_3 at the alloy GBs, (ii) the intermetallic phase δ-Ni_3(Nb,Mo) dissolves in the near-surface region and re-precipitates at the oxide-metal interface [43]. After 1000 h, the alloy grains coarsened in the subsurface dissolution zone of the CM specimen.

The AM specimens grew a morphologically similar external Cr_2O_3 scale and also revealed a characteristic re-precipitation of the δ-phase below the scale. However, the precipitate dissolution zone is less pronounced. The main microstructural difference between CM and AM are the subsurface voids in the AM specimens as previously reported for AM alloy IN625 [19–23]. The Cr_2O_3 scales on both CM and AM are undulant and corrugated. At the same time, the AM specimens do not reveal oxide ridges sticking out over the alloy GBs as in e.g. [22,23].

The corresponding EDX element mappings of the key elements involved in the oxidation process are presented in Fig. 6 (24 h) and Fig. 7 (1000 h). The O and Al maps visualize internal oxidation of Al at the GBs in CM and in the voids in the AM specimens. Particles containing Ti are detected in the Cr_2O_3 scale. Si was detected by EDX at the oxide-metal interface as well as in the voids. It should me mentioned that Si present in the void may be an artefact due to the final cross-section polishing step with colloidal silica. Most remarkably, Cr is not present in the voids. The subsurface porosity remains closed, and oxidation of the voids is limited to internal oxidation of Al. Minor traces of chromium

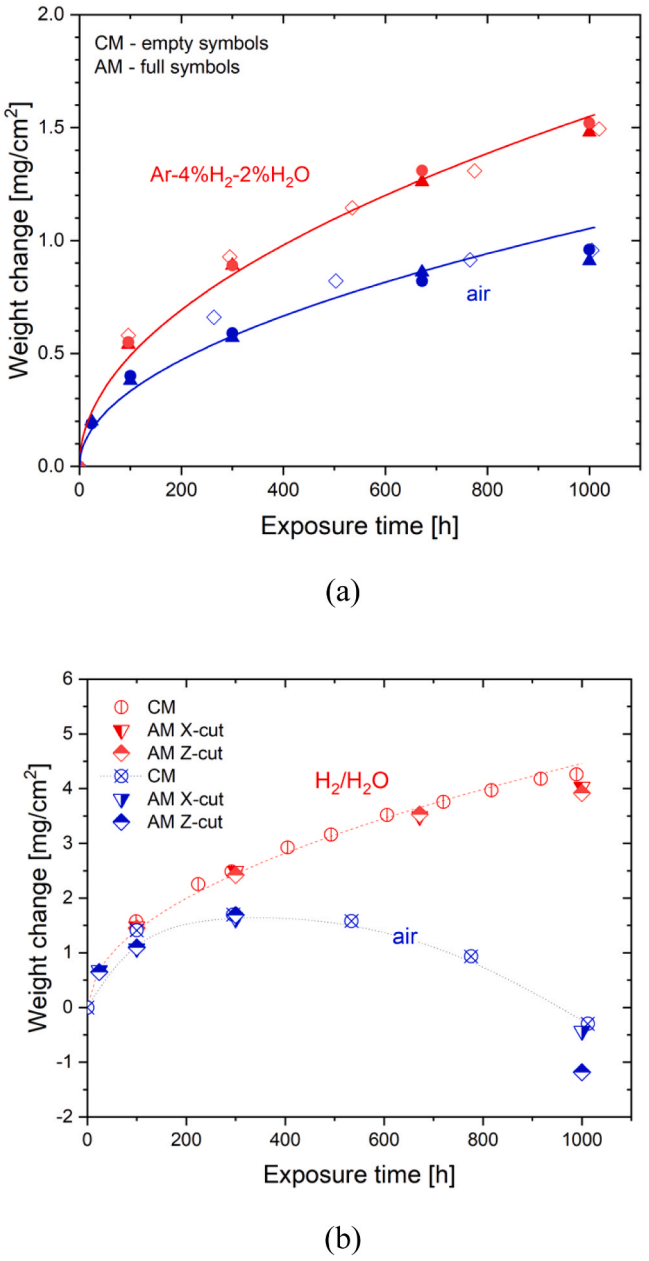

Fig. 4. Weight change curves recorded discontinuously for AM (full symbols) and CM (empty symbols) alloy IN625 exposed in stagnant lab air (in red) and Ar-4 %H_2-2 %H_2O gas mixture (in blue) for up to 1000 h at (a) 900 °C and (b) 1000 °C.

oxide can be found in some voids in the immediate vicinity of the oxide-metal interface after 1000 h in air at 900 °C. However, Cr oxidation neither propagated inwards nor resulted in IGOA.

Fig. 8 shows GD-OES profiles of the minor deoxidant alloying elements Al, Mn, Si and Ti in the CM and AM alloy IN625 specimens after 100 h oxidation in air at 900 °C. The profiles of the elements penetrating the Cr_2O_3 scale, i.e. Mn and Ti, have a very similar shape in the CM and AM specimens. The oxidation of Ti and Mn in IN625 is thus not affected by AM. Remarkably, Ti has two distinct enrichment peaks at both interfaces of the Cr_2O_3 scale (see also Fig. 6 and Fig. 7). This implies that some TiO_2 should be present at the oxide-metal interface or Ti could be incorporated into the Cr_2O_3 scale at the oxide-metal interface due to a higher solubility of Ti at low pO_2 [45]. Al and Si oxidize internally. The concentration profiles of Si and Al in CM and AM are similar. Both Al and Si reveal an enrichment peak at the oxide-metal interface in the CM and AM variants of the alloy. No such Si-enrichment in AM could be detected for a Si-low batch of AM alloy IN625 in [23,46]. The internal oxidation zone (Al) of Al in CM and AM are equally deep in agreement with SEM/EDX (see e.g. Fig. 6 and Fig. 7).

EBSD maps in Fig. 9 reveal a characteristic distribution of grain size in the Cr_2O_3 scales thermally grown on alloy IN625. After 24 h of exposure, the grain size distribution across the scale thickness is relatively uniform. After 1000 h, the oxide scale contains larger grains in the outer part and finer grains in the inner part close to the oxide-metal interface. Such a grain size distribution is indicative of a predominantly outward oxide growth. The Cr_2O_3 scale grown on the AM specimens appears to be more fine-grained in the innermost part and more corrugated in general. The AM specimens revealed more M_6C precipitates close to the oxide-metal interface, which is presumably related to a higher carbon content in AM compared to CM because of the AM process resulting in an increased content of interstitial elements such as O, N, and C [47] (Table 1).

Fig. 10 presents Kernel average misorientation (KAM) maps in the CM (a) and AM (b,c) in alloy IN625 after air oxidation for 1000 h at 900 °C. In the CM specimen, the KAM values are high (light green contrast vs dark blue background) only at the GBs in the oxidation affected zone where internal precipitation of Al_2O_3 took place (Fig. 7 and Fig. 8). Contrary to CM, the AM specimens reveal a dense network of lattice misorientations across the entire material, which is common for AM alloys [48]. An increased value of the Kernel average misorientation indicates a locally increased density of defects and stresses. The latter affect the diffusion properties of the AM alloy.

Fig. 11 shows SEM BSE images of cross-sectioned CM and AM alloy IN625 specimens exposed in Ar-4 %H_2-2 %H_2O for 1000 h at 900 °C (a, b, c) and 1000 °C (d, e, f). The Cr_2O_3 scales grown in Ar-4 %H_2-2 %H_2O are much smoother and slightly thicker compared to those grown in air (compare results for 900 °C with Fig. 5). The phase transformations at 900 °C (Fig. 11**a-c**) are identical to those observed in the air exposed specimens (Fig. 5**d-f**), i.e., dissolution and re-precipitation of the δ-phase. At 1000 °C, δ-phase is dissolved in the alloy IN625, but it precipitates at the oxide-metal interface as described in [38]. The alloy is, however, not single-phase at 1000 °C as M_6C carbide is stable. This carbide dissolves in the near-surface region during oxidation [38], which was observed in the present study in both CM and AM specimens. As the δ-phase is not pinning the alloy GBs at 1000 °C, the alloy grains coarsen substantially (from 5 to 50 μm over 1000 h at 1000 °C) in the CM specimen but not in AM (Fig. 11**e,f**). Finally, abundant subsurface porosity was found in the AM specimens at both temperatures.

3.4. Kinetic parameters

Fig. 12 shows the temporal evolution of the Cr_2O_3 scale thickness during oxidation in air and Ar-4 %H_2-2 %H_2O at 900 °C and 1000 °C measured from the SEM images. The metallographic analysis reveals no measurable difference in oxide growth kinetics between CM and AM in both gases in excellent agreement with in-situ TG (Fig. 3) and discontinuous furnace exposures (Fig. 4) except the air exposures at 1000 °C due to oxide spallation (not presented here). The parabolic rate constants, k_p calculated based on Eq. (1) and the data in Fig. 12 are summarized in Table 2 along with the literature data and Cr interdiffusion coefficients for alloy IN625.

$$X^2 = 2k_p t \quad (1)$$

The measured k_p values are in very good agreement with the previous measurements for the studied alloy batch [38] and literature data in general (see e.g. Fig. 5 in [22]).

Fig. 13 presents the temporal evolution of the void depth in AM alloy IN625 during oxidation in Ar-4 %H_2-2 %H_2O at 900 °C and 1000 °C measured from the SEM images. The void propagation kinetics are parabolic and, hence, diffusion controlled. The parabolic rate constants

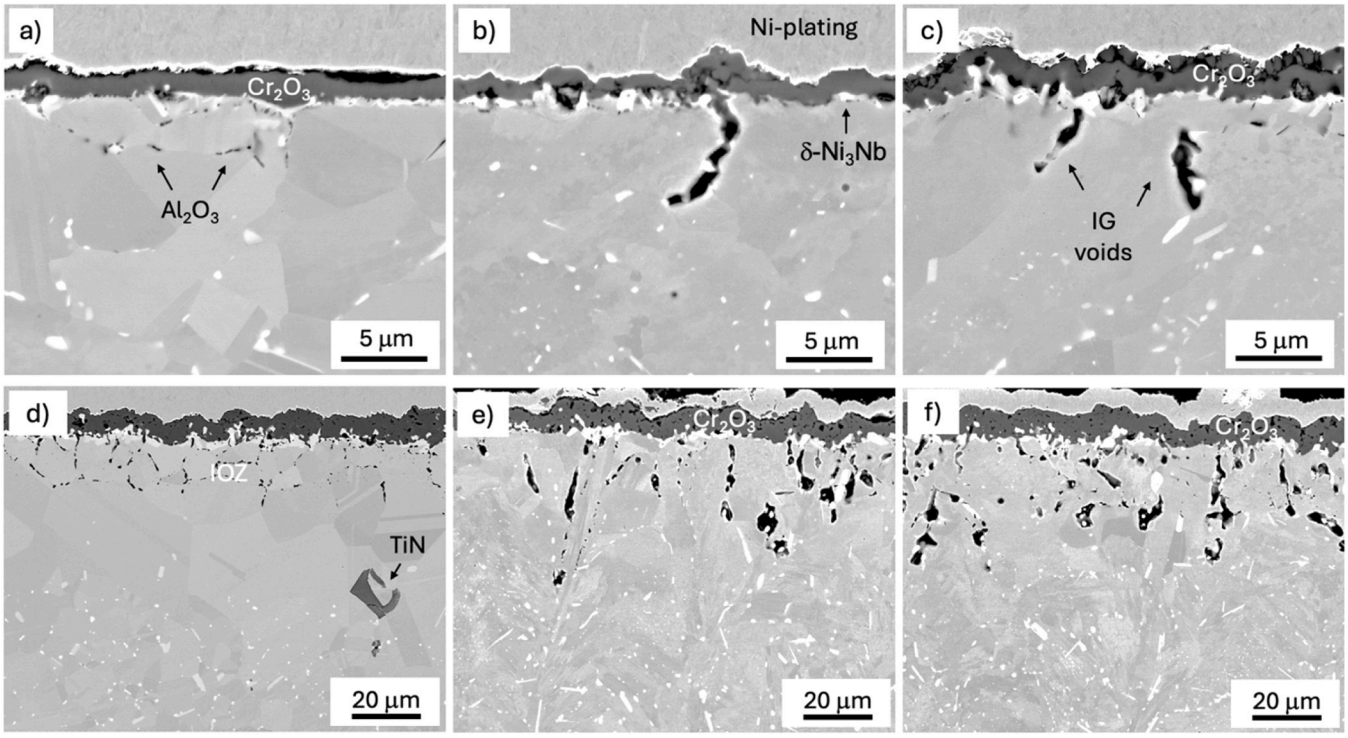

Fig. 5. SEM BSE images of oxide scales grown on CM (a,d) and AM-X (b,e) and AM-Z (c,f) alloy IN625 specimens after air exposure for 24 h (a,b,c) and 1000 h (d,e,f) at 900 °C.

calculated using Eq. (1) are 2.3×10^{-16} m^2 s^{-1} at 900 °C and 8.1×10^{-16} m^2 s^{-1} at 1000 °C, which is close to Cr diffusion coefficients in the alloy at the respective temperatures (Table 2).

3.5. Cr depletion

Cr depletion profiles measured with EDX in the CM and AM alloy IN625 specimens are shown in Fig. 14 (900 °C) and Fig. 15 (1000 °C). The experimental measurements (symbols) are compared with the calculated Cr-profiles obtained using the classical Wagnerian selective oxidation model [49]. For a binary alloy A-B in which only B reacts with oxygen while A is noble, the mole-fraction of B in the alloy, N_B, can be expressed as a function of distance from the oxide-metal interface z in m, time t in s:

$$\frac{N_B - N_B^{int}}{N_B^0 - N_B^{int}} = \frac{erf\left(z \Big/ \left[2\sqrt{\widetilde{D}_B t}\right]\right) - erf\left(\frac{k_c}{2D_B}\right)^{\frac{1}{2}}}{erfc\left(\frac{k_c}{2D_B}\right)^{\frac{1}{2}}} \quad (2)$$

here N_B^0 is the mole-fraction of B in the alloy bulk, i.e., initial concentration of B. N_B^{int} is the mole-fraction of B at the oxide-metal interface.

The kinetic parameters in Eq. (2) are parabolic rate constant, k_c, in m^2 s^{-1} expressed in terms of metal recession and interdiffusion coefficient of B in alloy A-B, $\widetilde{D}_B$, in m^2 s^{-1}, respectively. The metal recession rate constant k_c is directly related to the oxide growth rate constant k_p via the Pilling-Bedworth ratio:

$$k_c = k_p\left(\frac{\overline{V}_m}{\overline{V}_{ox}}\right)^2 \quad (3)$$

here $\overline{V}_m$ and $\overline{V}_{ox}$ are molar volumes of metal B and its oxide involved in the oxidation reaction. For Cr in a Ni-base alloy and Cr_2O_3 these values are 7×10^{-6} m^3 $mole^{-1}$ and 15×10^{-6} m^3 $mole^{-1}$, respectively.

The value N_B^{int} is the time-indent concentration of B at the oxide-metal interface and is intrinsically related to the balance of the consumption rate of B, k_c, and its supply from the alloy, $\widetilde{D}_B$:

$$N_B^{int} = \left(\frac{\pi k_c}{2\widetilde{D}_B}\right)^{\frac{1}{2}} \quad (4)$$

The Cr depletion profiles in the CM alloy IN625 are well approximated with Eq. (2) for both 900 °C (Fig. 14**a**) and 1000 °C (Fig. 15**a**). The kinetic parameters employed in the calculation of the Cr depletion profiles are summarized in Table 2. The Cr concentration at the oxide-alloy interface at 900 °C in CM is approximately 15 wt% in agreement with [38] and drops to 7 wt% in the specimens exposed in Ar-4 %H_2-2 % H_2O at 1000 °C.

In AM alloy IN625, the Cr depletion profiles remarkably differ from those in the respective CM specimens. The interface concentrations of Cr are higher, 17.0 vs 15.0 wt% at 900 °C (Fig. 14) and 13.0 vs 7.0 wt% at 1000 °C (Fig. 15). Considering that the oxidation rate constants, k_p, for CM and AM are identical (Fig. 3 and Fig. 12), it can be concluded that Cr diffusion is accelerated in AM compared to CM. The approximated $\widetilde{D}_{Cr}$ values for AM are summarized in Table 2. $\widetilde{D}_{Cr}$ is higher in AM relative to CM by a factor of 2 at 900 °C and factor of 3 at 1000 °C.

4. Discussion

4.1. Intergranular oxidation attack

The most striking and important finding in the present study is the absence of intergranular oxidation attack (IGOA) in the AM specimens (see e.g. Fig. 6 and Fig. 7). With a few exceptions [27,29], AM alloys IN625 [19–26] and IN718 [32–34] are generally reported to suffer from IGOA during oxidation at 900–1000 °C. IGOA occurring in AM Ni-base alloys [19–37] is usually discussed in literature in terms of comparing AM vs CM for which IGOA is not common. This study as well as experiments in [27,29] demonstrate that such a comparison can be made even between different AM batches of e.g. alloy IN625. The oxidation

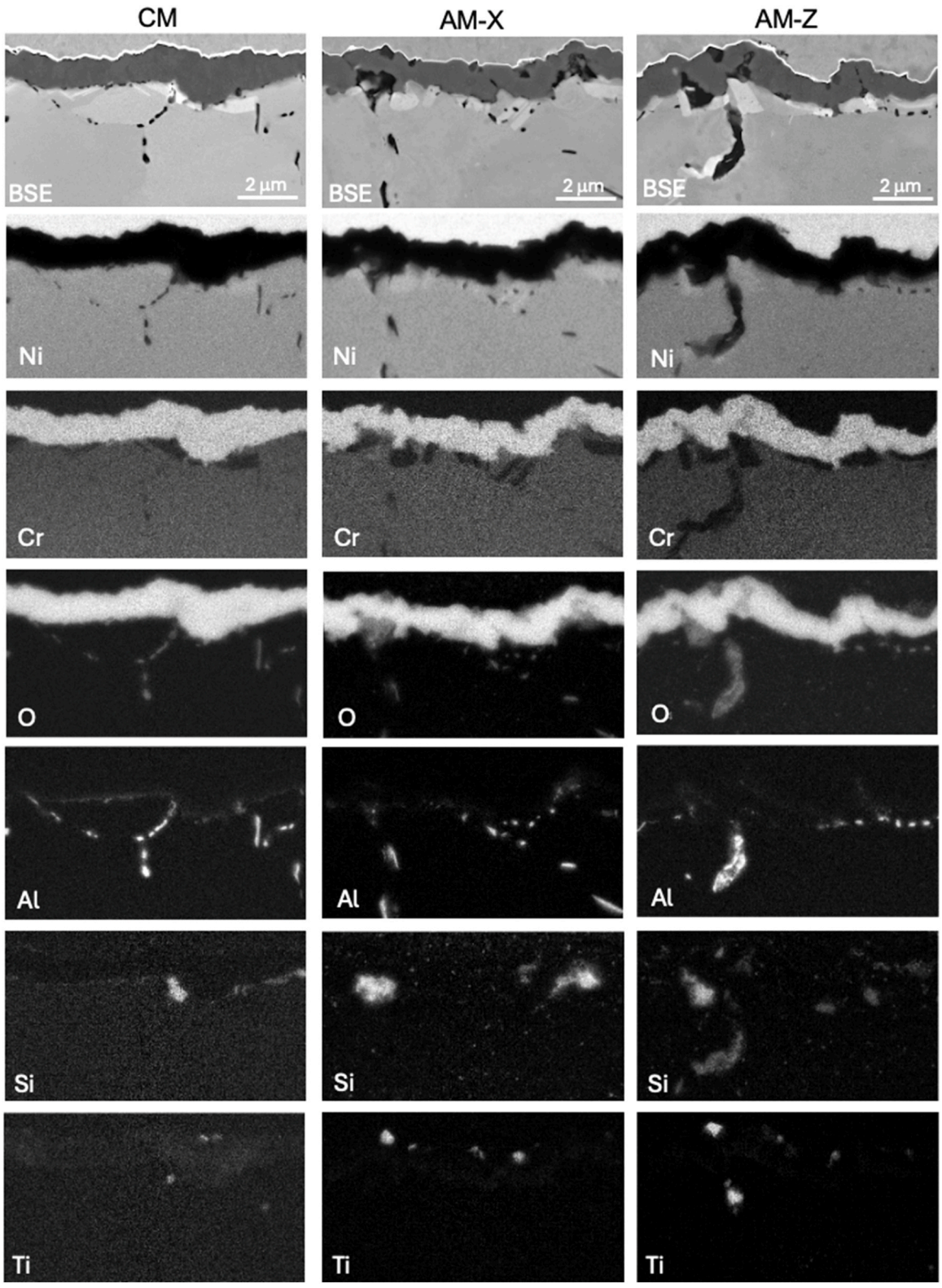

Fig. 6. EDX element maps of oxide scales grown on CM and AM alloy IN625 specimens after 24 h air exposure at 900 °C.

kinetics measurements in Fig. 3 and Fig. 4 show that IGOA is not necessarily triggered exclusively by AM, which undoubtedly has a strong effect on the alloy microstructure, transport properties in the alloy and, hence, its oxidation behavior. A common denominator for all reported oxidation studies of AM Ni-base alloys is the oxidation-induced subsurface porosity. The present study is not an exception, i.e., voids formed in the exposed AM specimens (Fig. 5 and Fig. 11): the spherical Kirkendall cavities within the alloy grains as well as strings of intergranular voids along the GBs.

Chyrkin et al. [46] proposed a decohesion mechanism of IGOA in which the key step initiating the process of accelerated oxidation is the decohesion and buckling of the Cr_2O_3 scale over the GBs of the alloy. The

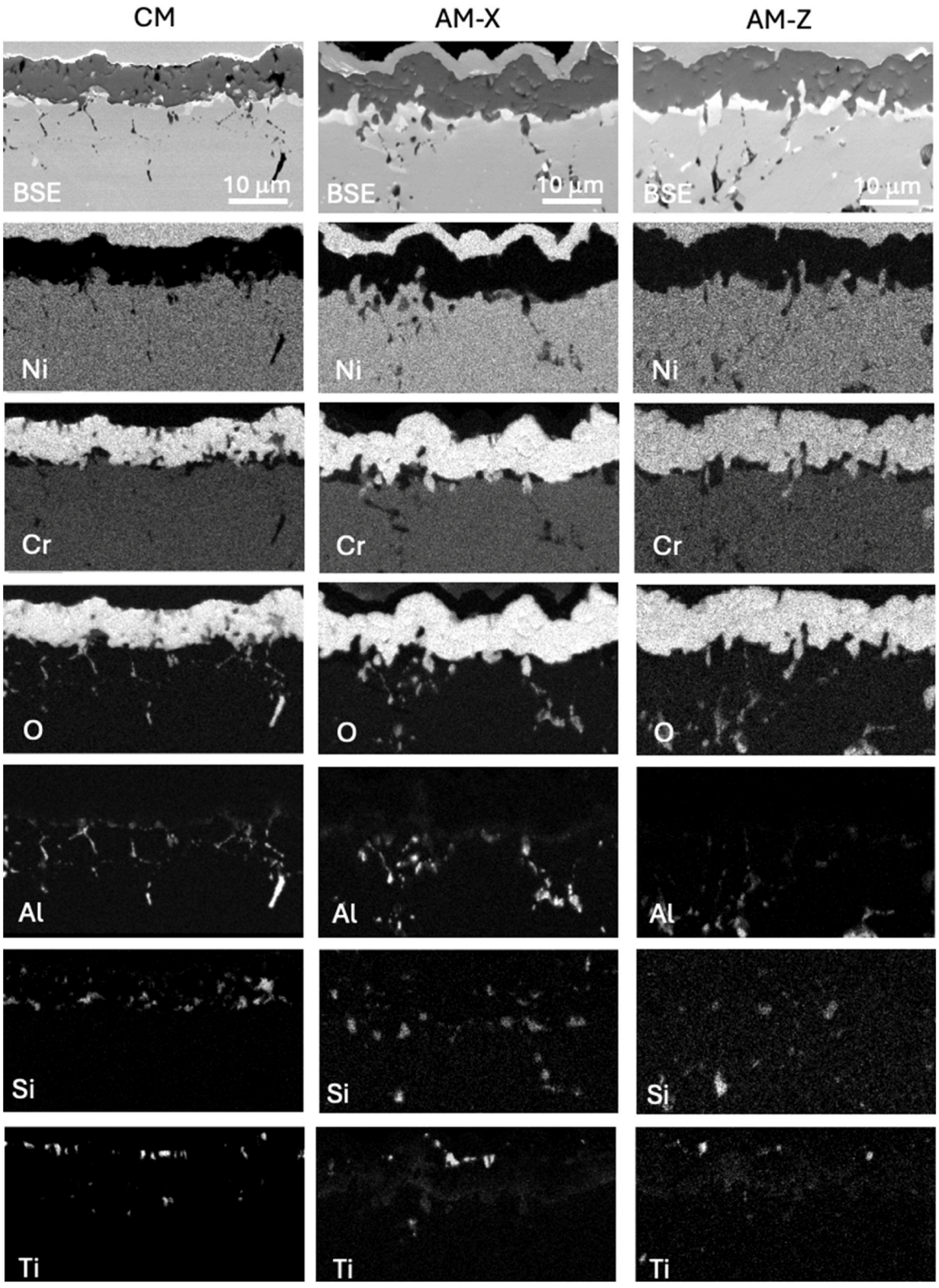

Fig. 7. EDX element maps of oxide scales grown on CM and AM alloy IN625 specimens after 1000 h air exposure at 900 °C.

spacing between the buckled oxide and the alloy substrate is then filled with the gas from the atmosphere, most likely through microcracks in the Cr_2O_3 scale as proposed by Gibbs in [50]. The alloy underneath the oxide buckle is re-oxidized, which intensifies the Cr depletion in the intermediate vicinity of the GB. The elongated intergranular voids form at the alloy GBs due to faster Cr diffusion (Table 2) in the AM alloy. The latter causes a flux of vacancies arising from the mismatch of Cr and Ni fluxes and eventual condensation of these vacancies at the alloy GBs. Cr diffusion in the AM alloy will be separately discussed in the next section.

When these two parallel and independent processes, i.e., oxide decohesion and void formation, occur simultaneously, intergranular voids at the oxide-metal interface open and oxidize. The voluminous

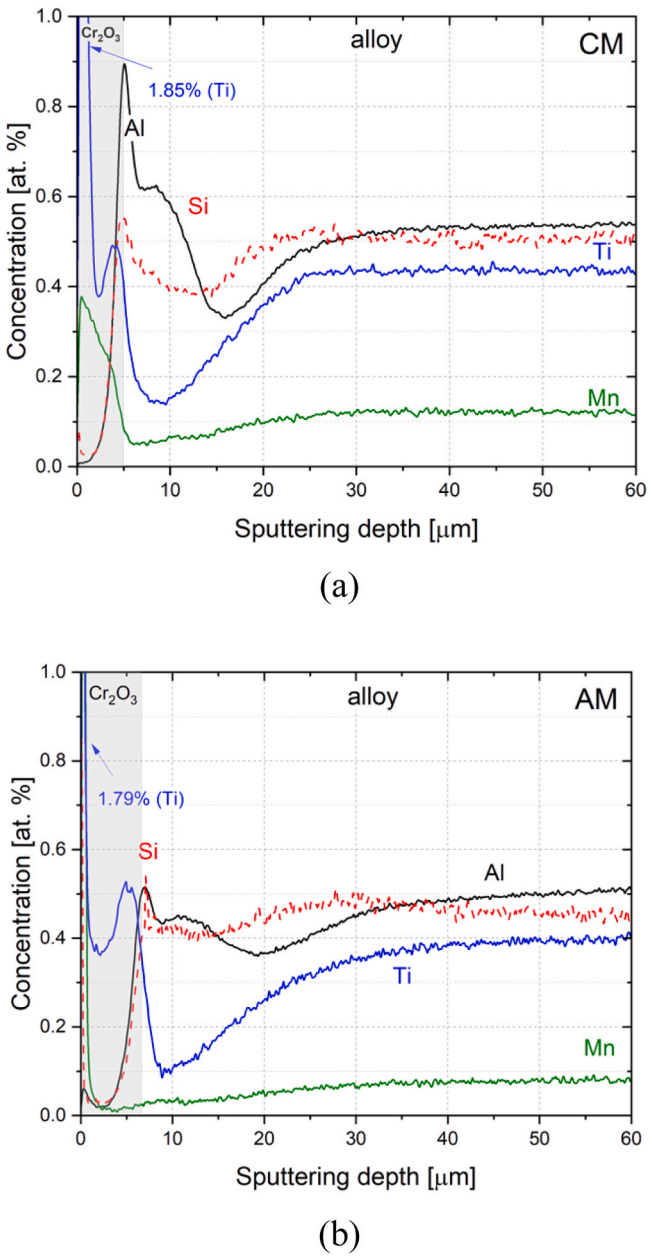

Fig. 8. GD-OES concentration profiles of Al, Mn, Si and Ti in (a) CM and (b) AM-Z alloy IN625 after 100 h oxidation in air at 900 °C.

internal Cr_2O_3 mass growing in these voids further cleaves the alloy along the GB and promotes thereby IGOA. From this perspective, the IG voids will not oxidize if the Cr_2O_3 scales remain well-adherent and do not buckle, i.e., IGOA will not occur if a massive oxide decohesion is prevented. The abundant subsurface porosity will be present in the oxidation affected zone of the AM alloy, but these voids will remain closed and will not be exposed to oxidation. The latter is systematically observed in the present work in both air and Ar-4 %H_2-2H_2O at 900 and 1000 °C. The Cr_2O_3 scale grown e.g. in air at 900 °C is corrugated as it formed under high compressive growth stresses (Fig. 5), however, it lacks any sign of a massive scale decohesion due to these stresses. At the same time, the elongated IG voids are present in the immediate vicinity of the oxide-metal interface. After 1000 h at 900 °C, these voids in the currently studied AM specimens are filled only with Al_2O_3 due to internal oxidation contrary to the observations with other AM versions of IN625 e.g. [22–25], where such IG voids are shown to be filled with Cr_2O_3. It should be noted that due to a higher thermodynamic stability of Al_2O_3 compared to Cr_2O_3, formation of Al_2O_3 internal precipitates may occur by a different mechanism, i.e. by oxygen dissolved interstitially from the adherent Cr-oxide scale into the metal whereby no access of molecular oxygen to the pore is required. Formation of alumina within the pores in the presently studied AM IN625 batch might be related to easier nucleation of precipitates at the pore walls than within the alloy grain similar to the process occurring at the alloy grain boundaries of CM IN625 [38] at the oxide-metal interface as demonstrated e.g. for alloy 617 in [51].

The absence of IGOA in the present work is also reflected in oxidation kinetics. Both thermogravimetry (Fig. 3 and Fig. 4) and the metallographic analysis (Fig. 12) demonstrate that the oxidation rates of currently studied AM and CM are virtually identical as IGOA is the only essential contributor to the accelerated oxidation of other AM IN625 alloy versions.

Finally, the decohesion mechanism is supported by another work of Chyrkin et al. [52], in which a batch of AM alloy IN625 suffering from IGOA was coated with 10 nm Ce to increase oxide adherence. Small additions of reactive elements (RE) such as Ce, Y, La are well known to improve corrosion resistance of Cr_2O_3 and Al_2O_3 forming high-temperature alloys via i) lowering the oxide growth rate and ii) improving oxide adhesion. Both effects were achieved by applying the Ce-coating. Most interestingly, the Cr_2O_3 scale on the Ce-coated alloy adhered very well and did not buckle over the GBs. Even though coating with Ce dramatically reduced the overall oxidation rate of AM alloy IN625 and thus the extent of subscale porosity, the IG voids still were present underneath the oxide scale. However, these voids neither opened nor oxidized and contained only internally precipitated Al_2O_3.

The experimental results obtained in the present study together with the relevant case-studies in literature [27,29], especially the RE effect [52], validate the decohesion mechanism [46] of IGOA occurring in AM Ni-base alloys, i.e., IGOA does not occur if oxide scale delamination is prevented. This raises an extremely important question why the Cr_2O_3 scales thermally grown on some specific batches of AM alloy IN625 are prone to decohesion while apparently the same Cr_2O_3 scales can be well-adherent to the metal when grown on other AM alloy batches? The factors affecting oxide adhesion to the alloy substrate will be addressed in the following sections.

4.2. Oxide adhesion

This study was designed to differentiate the AM effects from the batch-to-batch variation effects on the oxidation behavior of AM alloy IN625 and single out the main trigger of IGOA. As demonstrated in the present study (Fig. 12) and also in [46], the Cr_2O_3 growth kinetics was not affected by AM while the abundant subscale porosity in the AM specimens did not develop into IGOA when the AM alloy was manufactured from the same alloy batch as CM and had the same chemical composition (Table 1). The most evident difference between AM and CM established in the present work is the adhesion of the Cr_2O_3 scale to the alloy substrate. Oxide adhesion to the underlying metal is an important and well-explored property of technically relevant high-temperature alloys [53–55]. The focus in the available literature on adhesion of Cr_2O_3 and Al_2O_3 scales is made on i) its sensitivity to minor alloying elements [53,55,56], ii) the beneficial effect of reactive elements (RE) such as Y, Ce, La [57–60], iii) the detrimental role of interstitial impurities such as C and S segregating to available interfaces [59], iv) improved oxide adhesion mechanisms such as “pegging” or “keying” [59,61,62] as well as v) developing experimental techniques to quantify the adhesion energy [53–56]. In the context of the present study, the effect of minor alloying elements as well as oxide pegs affected by these minor elements appear most relevant.

Mn is ubiquitous in high-temperature alloys. High concentrations of Mn are usually detrimental for oxidation behavior [63,64]. However, minor alloying with Mn up to approximately 0.3 wt% is known to promote the formation of an external $MnCr_2O_4$ layer which hampers

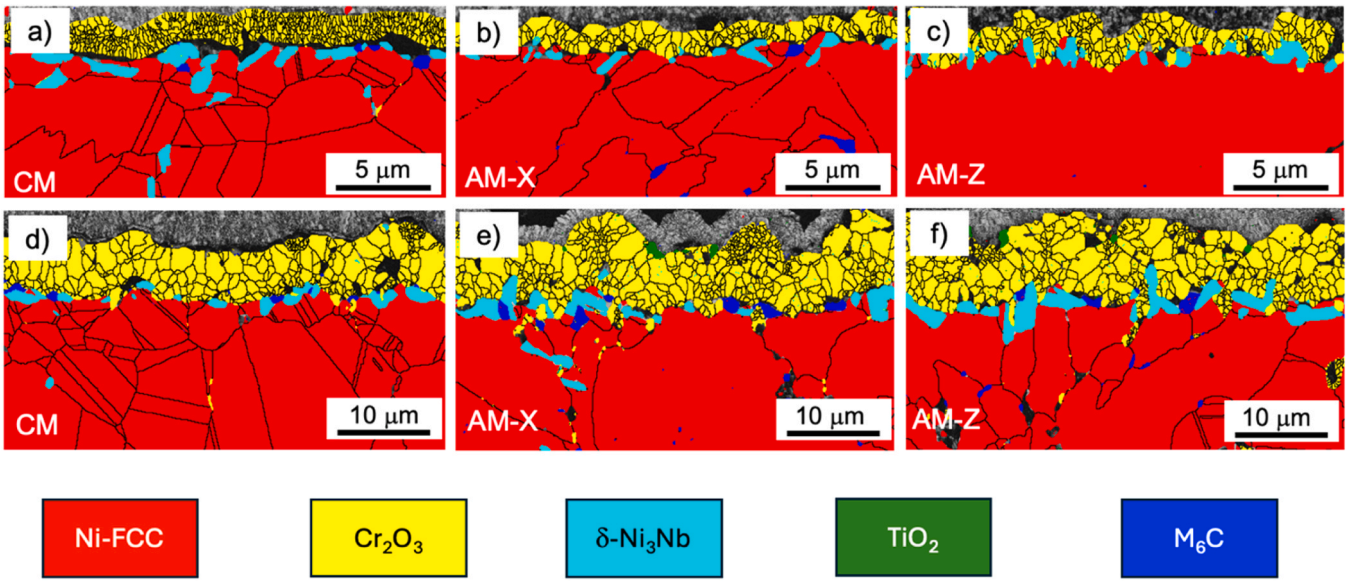

Fig. 9. EBSD maps of oxide scales grown on CM (a,d) and AM-X (b,e) and AM-Z (c,f) alloy IN625 specimens after air exposure for 24 h (a,b,c) and 1000 h (d,e,f) at 900 °C.

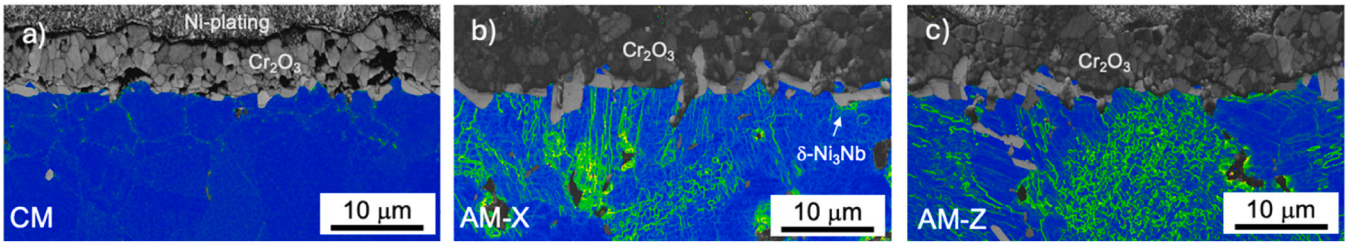

Fig. 10. Kernel average misorientation (KAM) maps in γ-FCC of (a) CM, (b) AM-X and (c) AM-Z alloy IN625 specimens after 1000 h air oxidation at 900 °C.

reactive evaporation of Cr_2O_3 in humid gases [65,66]. At low concentrations, Mn tends to diffuse through the Cr_2O_3 scale (see the Mn profiles in Fig. 8), does not segregate at the oxide-metal interface and thus marginally affects the adhesion of Cr_2O_3. Nanoparticles of Mn-rich oxides were recently detected by atom probe tomography (APT) precipitated inside the grains of the Cr_2O_3 scale grown on CM IN625 [46]. These particles presumably formed during the initial stages of oxidation of all elements available in the alloy before the alloy surface was fully covered with Cr_2O_3.

The GD-OES profiles of Ti, Al and Si in Fig. 8 demonstrate clear enrichment peaks at the oxide-metal interface indicating precipitation of the corresponding oxide particles at this boundary. The signals of Ti, Al and Si-rich particles at the oxide-metal interface can be also discerned in the EDX concentration maps (Fig. 6 and Fig. 7) even though the resolution of the maps is weak due to low concentrations of these alloying elements.

The minor alloying elements are known to affect the Cr_2O_3 adhesion. Mougin et al. [55] demonstrated a beneficial effect of TiO_2 particles pegging the Cr_2O_3 scale grown on ferritic stainless steel. Hou and Stringer [61] reported a positive effect of Al ion implantation on the adhesion of Cr_2O_3 on a binary model alloy Ni-25Cr. A beneficial effect of alloying FeCr- and NiCr-based alloys with minor amounts of Al is reported in other studies [67–69].

The effect of Si addition on the oxide scale adhesion is complex and rather contradictory. Si is generally believed to improve the performance of chromia-forming alloys [39,70] via lowering the scaling rate. However, SiO_2 forming a subscale is often found to increase the risk of oxide spallation [40–42,56,71]. Similar to Mn, high levels of alloying with Si are detrimental. At the same time at low concentrations (0.2–0.3 wt%), Si is reported to segregate to the oxide-metal interface [72] and significantly improve oxidation behavior [70]. Low concentrations of Si might be beneficial as well for Cr_2O_3 adhesion as e.g. those of Al and Ti. The APT analyses of the oxide-metal interfaces in CM IN625 (the batch used in the present study) after 1000 h air oxidation at 900 °C [46] revealed no Si peak at the oxide-metal boundary while the GD-OES profile of Si demonstrated a significant Si enrichment underneath the Cr_2O_3 scale. It is therefore highly likely that SiO_2 at the oxide-metal interface is also present in form of nano-sized particles as e.g. demonstrated with APT for a FeCr-base alloy in [73].

In summary, minor elements (Ti, Si, Al) present in alloy IN625 are reported to moderately improve the adhesion of Cr_2O_3 grown on Ni-Cr model alloys. It is reasonable to assume that changes in the chemical composition, with respect to these minor alloying elements, between CM and AM may result in deteriorated Cr_2O_3 adhesion, oxide decohesion and IGOA. AM alloy IN625 in [23,46] suffered from oxide buckling and IGOA. In contrast to the CM specimen, the GD-OES profiles did not reveal a subscale peak of Si as the AM batch had a lower Si content (0.08 wt%) compared to CM (0.24 wt%). In other cases of IGOA reported for AM alloy IN625 [19–21], the alloy Si content was also low (0.11 wt%). Several studies [24,25,31] either do not disclose the exact chemical composition of the AM material or give a nominal composition of alloy IN625.

It is presently not clear why many batches of AM Ni-base alloys have lower additions of elements such as Si or Al compared to CM versions of the same material. However, this seems to be not only a feature of Ni-base alloys, as lower Al-content was also observed in the AM-version compared to cast product of a Co-base superalloy [14]. It is possible that some loss of these minor additions occurs during powder

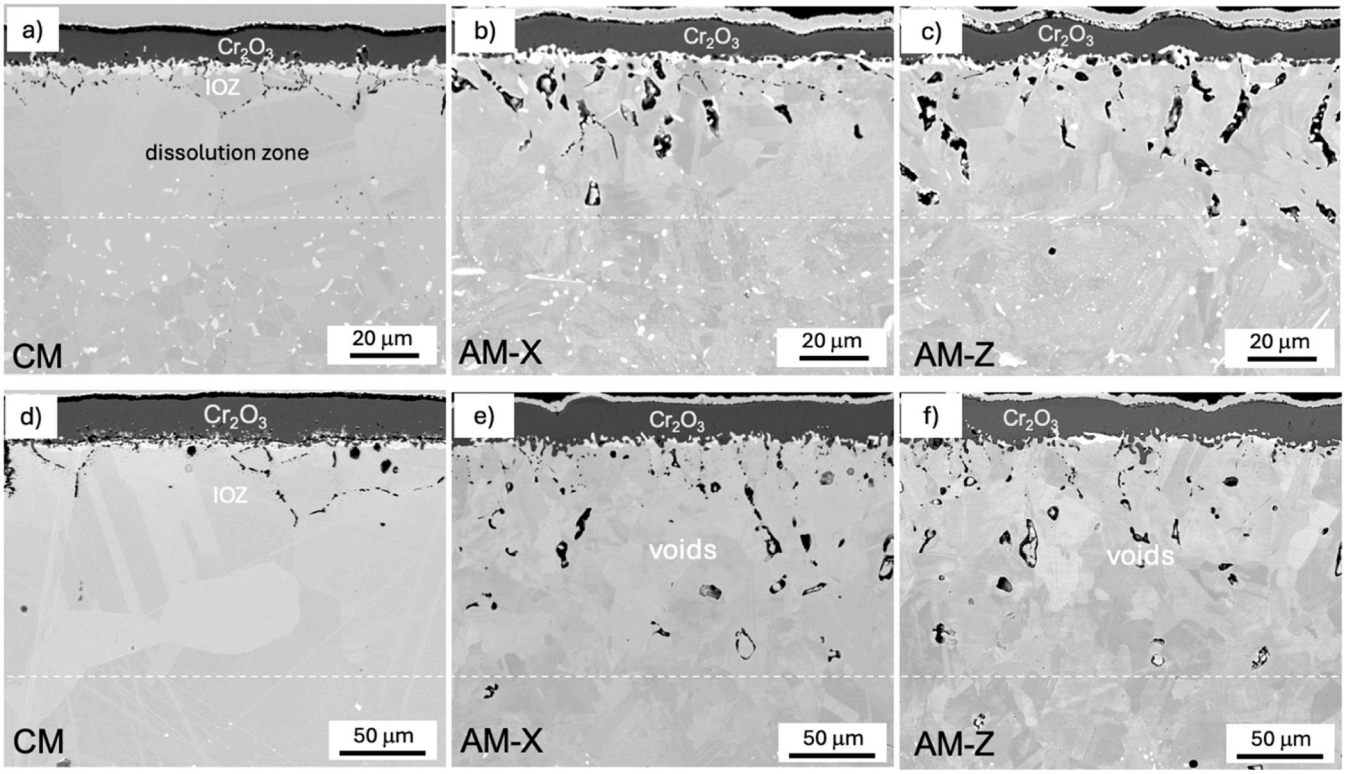

Fig. 11. SEM BSE images of oxide scales grown on CM (a,d) and AM-X (b,e) and AM-Z (c,f) alloy IN625 specimens after 1000 h exposure in Ar-4 %H_2-2 %H_2O at 900 °C (a,b,c) and 1000 °C (d,e,f). Note the difference in scale bars.

manufacturing or even that the Si (Al) contents are deliberately kept low by the powder manufacturers for a better processibility of the powders by AM. Anyway, the present study demonstrated that a preservation of the alloy chemistry during the AM process, i.e., minimal departures from the initial composition of the CM precursor (Table 1), resulted in a well-adherent, non-buckling Cr_2O_3 scale, which prevented the occurrence of IGOA despite the abundant intergranular porosity induced by AM.

4.3. Accelerated Cr diffusion

An important effect of AM in alloy IN625 observed in the present study is the enhanced diffusion of Cr in the alloy. The Cr depletion profiles in Fig. 14 and Fig. 15 along with the kinetic parameters summarized in Table 2 indicate two important findings:

i. There is no measurable Cr diffusion anisotropy in the AM alloy.
ii. Cr diffusion is accelerated in AM compared to CM by a factor of 2–3.

The accelerated Cr diffusion measured in AM alloy IN625 is not surprising. Even though the literature on diffusion in AM high-temperature alloys is rather limited, several studies report Cr depletion profiles in AM Ni-base alloys [16,17] and AISI 316 L [74,75] describing flatter Cr profiles in AM alloys compared to CM. In other words, Cr is systematically reported to diffuse faster in AM than in CM alloys. Based on the reported Cr depletion profiles [74,75], an average acceleration factor of 2 can be estimated, which agrees well with the findings in this study (Table 2). The acceleration of Cr diffusion manifests itself in an increased interface Cr concentration as well as in a deeper Cr depletion front and should be attributed to the additive microstructure of the alloy. The characteristic melt pools (Fig. 1**a,c)** in the AM microstructure of the alloy contain sub-micron dendritic cells (Fig. 1**b,d**) which provide the material with a dense network of additional GBs. Fig. 10 demonstrates the difference between CM ad AM in this regard, i.e., the density of lattice misorientations is clearly higher in the AM specimens compared to the CM one. More importantly, these dendritic cells survive the 1000 h exposure at 900 °C as shown in Fig. 16**a**.

Furthermore, the AM effect on Cr diffusion in the present work appears stronger at 1000 °C, the acceleration factor amounting to 3 (Table 2) compared to factor of 2 at 900 °C. This additional acceleration of Cr diffusion in AM may be attributed to the different grain coarsening dynamics in AM and CM at this temperature. At 1000 °C, the δ-Ni_3Nb phase is not stable and completely dissolved in the Ni-matrix while it is stable at 900 °C [38]. This phase tends to precipitate at the GBs and hampers alloy grain coarsening by pinning them below 930–980 °C. The alloy grains in alloy IN625 can also coarsen at 900 °C providing that the δ-Ni_3Nb phase is dissolved as e.g. in the oxidation affected zone (see Fig. 5**d**). This precipitate dissolution mechanism applies both to CM and AM.

However, the alloy grains in AM do not grow as they do in CM at 1000 °C (compare fig. d with figs. e and f in Fig. 11) even though δ-Ni_3Nb phase is completely dissolved in both CM and AM. The impeded grain coarsening can be seen as well in the high-magnification image of the AM alloy microstructure after 1000 h at 1000 °C in Fig. 16b. Event at 1000 °C, the sub-micron grains coarsen to a few µm but not to 50–100 µm as in CM (Fig. 11**d**). This microstructural stability of AM is likely to be the consequence of a GB pinning by particles of TiN (black dots at the GBs in Fig. 16**b**) decorating the alloy GBs [76] resulting from nitrogen introduced during the AM process (Table 1). The GB network in AM remains thus stable and unaffected by grain coarsening during exposure at 1000 °C while the GB network in CM progressively shrinks. The dynamic reduction of the GB contribution of alloy Cr diffusion in CM is thus believed to increase the difference in net Cr diffusion between AM and CM alloy IN625. Recent studies [77] demonstrate that the GB contribution to Cr diffusion in alloy IN 625 is significant even at 1000 °C.

Apart from different GB densities in AM and CM, AM alloys are also known to develop dense networks of dislocations in the microstructure

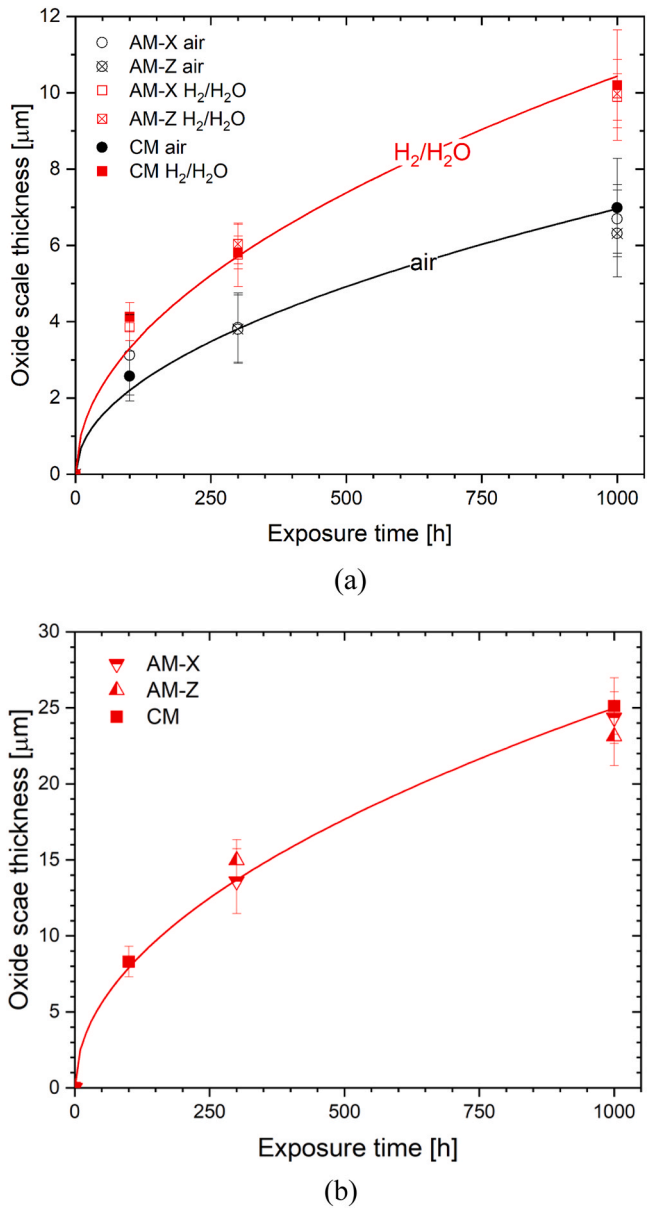

Fig. 12. Temporal evolution of oxide scale thickness measured from SEM images for CM and AM alloy IN625 exposed for up to 1000 h in air and Ar-4 %H_2-2 %H_2O at 900 °C (a) and 1000 °C (b). At 1000 °C, oxide thickness was measured only for the specimens exposed in Ar-4 %H_2-2 %H_2O. Air exposed specimens suffered from severe oxide spallation at 1000 °C. Lines are parabolic fits calculated using parameter summarized in Table 2.

[78–81] during atomizing and printing due to large thermal gradients, high cooling rates and a complicated thermal history. The accelerated transport over short-circuit paths can be affected by a phenomenon termed as dislocation pipe diffusion [82,83]. However, a systematic high-resolution microscopy study is required to confirm and/or quantify a contribution of dislocations to the overall acceleration of diffusion in AM.

Another remarkable consequence of enhanced Cr diffusion in AM is the higher concentrations of Cr at the oxide-metal interface in the AM specimens compared to CM (see Cr-depletion profiles in Fig. 14 and Fig. 15). This increased Cr-interface concentration might be the reason of a more abundant precipitation of δ-Ni_3Nb at the oxide-metal interface in AM compared to CM (Fig. 9) as Cr is known to stabilize δ-Ni_3Nb in IN625 [38].

Enhanced Cr diffusion in the AM alloy may have beneficial as well as detrimental effects on the oxidation resistance of the alloy. Faster Cr diffusion generally is viewed as a positive factor increasing Cr supply to the oxide-metal interface and thereby improving the resistance to breakaway oxidation [84,85]. It is often intentionally induced by cold-work [86] of the surface to promote protective oxidation [87,88]. At the same time, higher Cr fluxes through the network of alloy GBs and dislocation will produce an additional vacancy flow [89,90]. Together with the vacancies injected from the oxide growth process [51], this oversaturation of vacancies will further intensify the Kirkendall porosity in the Cr-depleted alloy subsurface [91]. During the exposures at 900 and 1000 °C, the voids formed exclusively in the oxidation affected, Cr-depleted zone and not in the alloy bulk. This implies that the subsurface voids are induced primarily by oxidation (Cr consumption) but not by the AM process *per se*. Another factor affecting the subsurface porosity are the stresses in the oxide scale that are known to intensify the void development [20].

In summary, the oxidation-induced subsurface porosity is inevitable

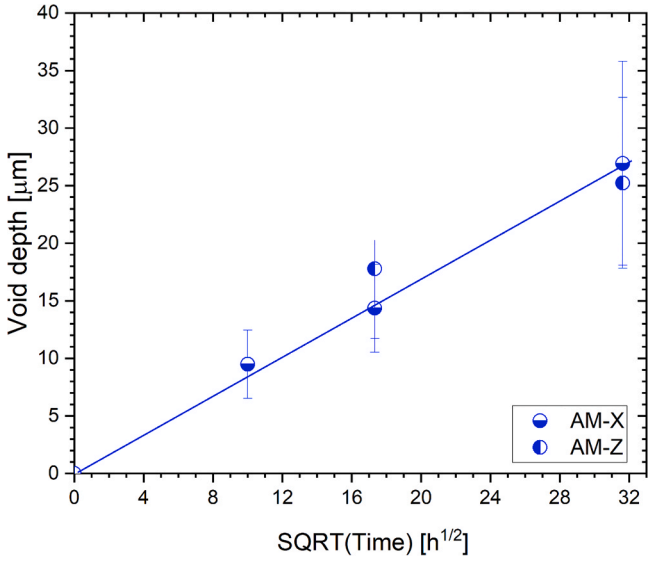

Fig. 13. Kinetics of void propagation in AM alloy IN625 measured SEM images for specimens exposed for up to 1000 h in Ar-4 %H_2-2 %H_2O at 900 °C.

Table 2
Parabolic rate constant, k_p, and interdiffusion coefficient of Cr, $\widetilde{D}_{Cr}$, in alloy IN625. The reference values for CM were taken from [38,77]. The experimental values for CM and AM were determined from the Cr depletion profiles.

T, °C	k_p^{exp} [$m^2\ s^{-1}$]	k_p^{lit} [$m^2\ s^{-1}$]	$\widetilde{D}_{Cr}^{lit,CM}$ [$m^2\ s^{-1}$]	$\widetilde{D}_{Cr}^{exp,CM}$ [$m^2\ s^{-1}$]	$\widetilde{D}_{Cr}^{exp,AM}$ [$m^2\ s^{-1}$]	k_p^{voids} [$m^2\ s^{-1}$]
air						
900	1.0×10^{-17}	8.0×10^{-18}	2.4×10^{-16}	2.5×10^{-16}	4.0×10^{-16}	2.2×10^{-16}
1000	1.1×10^{-16}	8.5×10^{-17}	5.0×10^{-16}	-	-	2.6×10^{-16}
Ar-4 %H_2-2 %H_2O						
900	1.9×10^{-17}	1.1×10^{-17}	2.0×10^{-16}	2.4×10^{-16}	5.0×10^{-16}	2.3×10^{-16}
1000	9.0×10^{-17}	1.0×10^{-16}	5.0×10^{-16}	5.8×10^{-16}	1.5×10^{-15}	8.1×10^{-16}

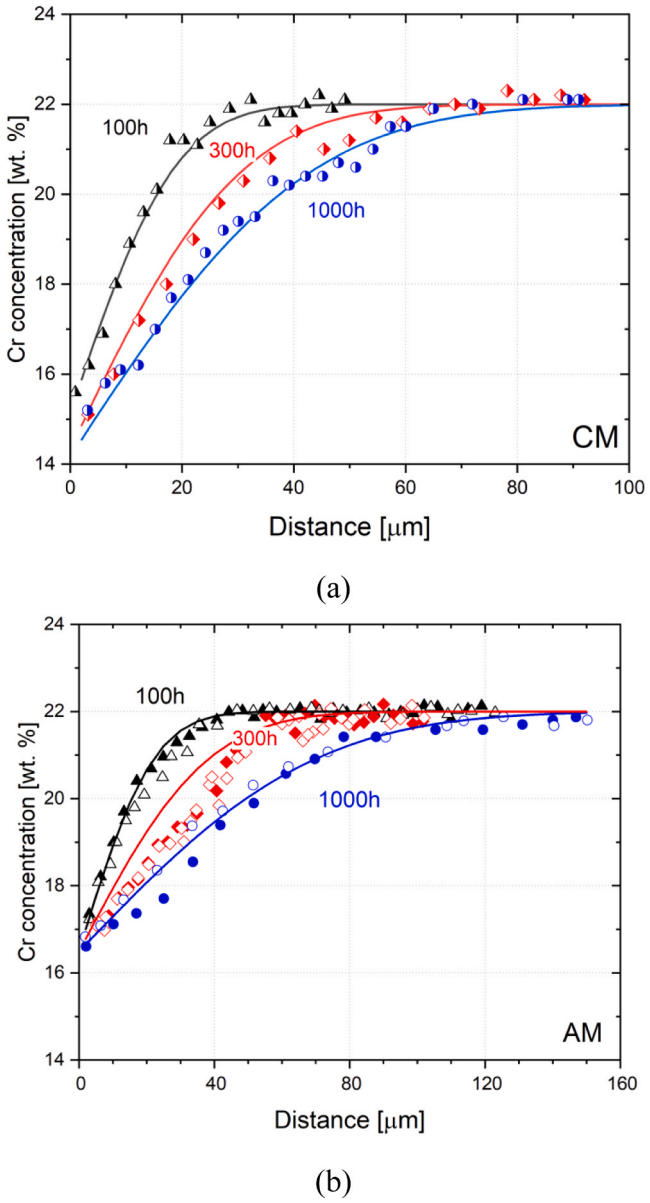

Fig. 14. Chromium concentration profiles in CM (a) and AM (b) alloy IN 625 after air oxidation at 900 °C measured by EDX (symbols) compared with calculated values (lines) using classical Wagner's theory [49]. The curves were calculated using $k_p = 1 \times 10^{-17}$ m^2 s^{-1}, $D_{Cr} = 2.5 \times 10^{-16}$ m^2 s^{-1} for CM (a) and $D_{Cr} = 4.0 \times 10^{-16}$ m^2 s^{-1} for AM (b). For AM alloy IN625 (b), full symbols denote AM-Z while empty ones denote measurements for AM-X.

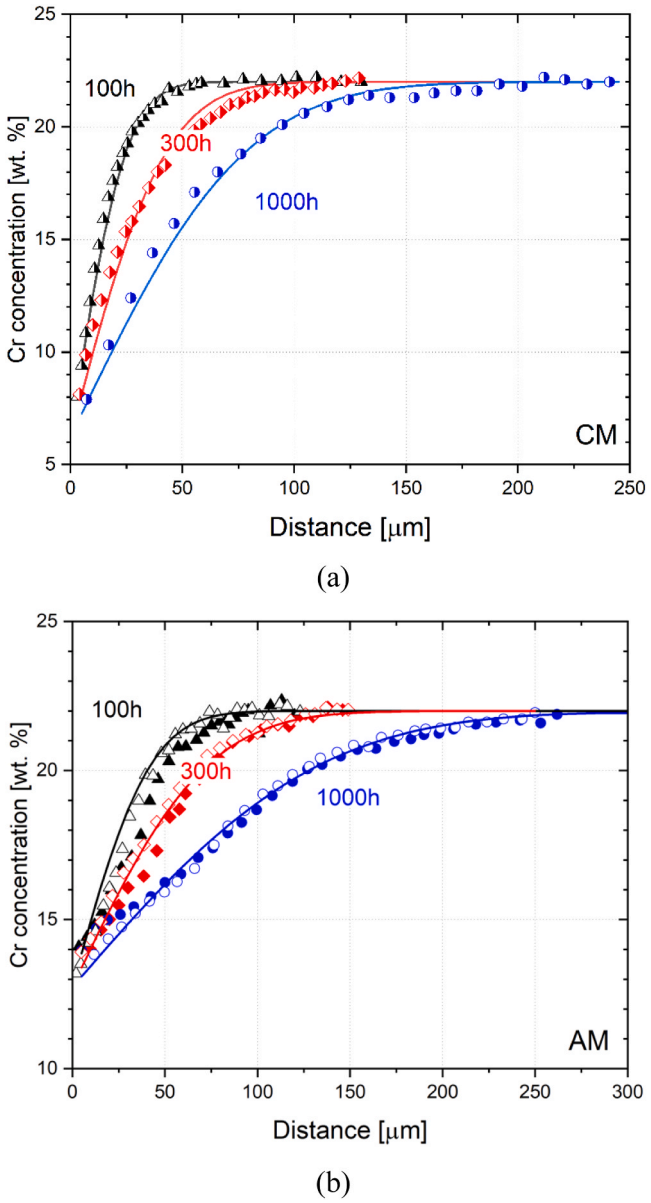

Fig. 15. Chromium concentration profiles in CM (a) and AM (b) alloy IN 625 after exposure in Ar-4 %H_2-2 %H_2O at 1000 °C measured by EDS (symbols) compared with calculated values (lines) using classical Wagner's theory [49]. The curves were calculated using $k_p = 9.0 \times 10^{-17}$ m^2 s^{-1}, $D_{Cr} = 5.0 \times 10^{-16}$ m^2 s^{-1} for CM (a) and $D_{Cr} = 1.5 \times 10^{-15}$ m^2 s^{-1} for AM (b). For AM alloy IN625 (b), full symbols denote AM-Z while empty ones denote measurements for AM-X.

in AM Ni-base alloys. However, the occurrence of porosity, both in-grain and IG, does not necessarily lead to IGOA. The key factor triggering IGOA is the Cr_2O_3 adhesion to the alloy, i.e., whether the subsurface voids will open or not.

5. Conclusions

This work demonstrates that additive manufacturing (AM) alone is not the ultimate trigger of intergranular oxidation attack (IGOA) of Ni-base alloys such as IN625. The following conclusions can be highlighted:

- AM has its reproducible effects on the microstructure and properties of high-temperature alloys such as enhanced diffusion and the ensuing oxidation-induced porosity. However, the subsurface intergranular porosity is an insufficient precondition of IGOA in AM alloy.
- The key factor of IGOA occurrence is oxide adherence to the alloy substrate. The latter is demonstrated using alloy IN625 to be related to the fine chemistry of the alloy, specifically the minor deoxidant elements e.g. Al, Si, Mn, Ti inevitably present in the metallurgy of Ni-base superalloys.
- AM is demonstrated to have no effect on oxidation kinetics and oxide adhesion providing that the chemical composition of the compared AM and CM alloy batches is virtually identical.

CRediT authorship contribution statement

A. Chyrkin: Writing – review & editing, Writing – original draft, Visualization, Validation, Supervision, Project administration, Methodology, Investigation, Funding acquisition, Formal analysis, Data

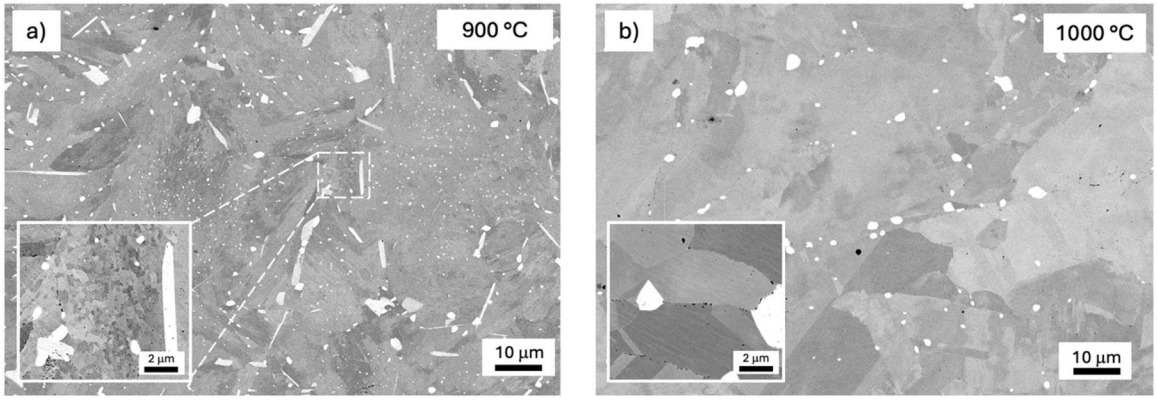

Fig. 16. BSE SEM micrographs of AM alloy IN625 in the middle of the specimen after 1000 h exposure at (a) 900 °C and (b) 1000 °C. The high-magnification inserts demonstrate the evolution of dendritic cells.

curation, Conceptualization. **J.-P. Roth**: Writing – review & editing, Resources, Methodology, Data curation. **D. Naumenko**: Writing – review & editing, Resources, Project administration, Conceptualization. **K. Jahns**: Writing – review & editing, Resources, Project administration, Conceptualization.

Declaration of Competing Interest

The authors declare that they have no known competing financial interests or personal relationships that could have appeared to influence the work reported in this paper.

Acknowledgements

This study received no funding. Mr. H. Cosler (FZJ) is acknowledged for performing the *in-situ* TG-experiments and Dr. E. Wessel (FZJ) for SEM/EBSD analyses, respectively.

Data availability

Data will be made available on request.

References

[1] R.C. Reed, The Superalloys, Cambridge University Press, 2006.
[2] H.L. Eiselstein, D.J. Tillack, The Invention and Definition of Alloy 625. Superalloys 718, 625 and Various Derivatives (1991), TMS, 1991, pp. 1–14.
[3] L.E. Murr, Metallurgy of additive manufacturing: examples from electron beam melting, Addit. Manuf. 5 (2015) 40–53, https://doi.org/10.1016/j.addma.2014.12.002.
[4] C.U. Brown, G. Jacob, M. Stoudt, S. Moylan, J. Slotwinski, A. Donmez, Interlaboratory study for nickel alloy 625 nade by laser powder bed fusion to quantify mechanical property variability, J. Mater. Eng. Perform. 25 (2016) 3390–3397, https://doi.org/10.1007/s11665-016-2169-2.
[5] T. DebRoy, H.L. Wei, J.S. Zuback, T. Mukherjee, J.W. Elmer, J.O. Milewski, A. M. Beese, A. Wilson-Heid, A. De, W. Zhang, Additive manufacturing of metallic components – Process, structure and properties, Prog. Mater. Sci. 92 (2018) 112–224, https://doi.org/10.1016/j.pmatsci.2017.10.001.
[6] G.P. Dinda, A.K. Dasgupta, J. Mazumder, Laser aided direct metal deposition of Inconel 625 superalloy: microstructural evolution and thermal stability, Mater. Sci. Eng. A 509 (2009) 98–104, https://doi.org/10.1016/j.msea.2009.01.009.
[7] W.E. Frazier, Metal additive manufacturing: a review, J. Mater. Eng. Perform. 23 (2014) 1917–1928, https://doi.org/10.1007/s11665-014-0958-z.
[8] K. Son, M.E. Kassner, K.A. Lee, The creep behavior of additively manufactured Inconel 625, Adv. Eng. Mater. 22 (2020), https://doi.org/10.1002/adem.201900543.
[9] K.-T. Son, T.Q. Phan, L.E. Levine, K.-S. Kim, K.-A. Lee, M. Ahlfors, M.E. Kassner, The creep and fracture properties of additively manufactured Inconel 625, Materialia 15 (2021) 101021, https://doi.org/10.1016/j.mtla.2021.101021.
[10] M.E. Kassner, K.T. Son, K.A. Lee, T.-H. Kang, R. Ermagan, The creep and fracture behavior of additively manufactured Inconel 625 and 718, Mater. High. Temp. 39 (2022) 499–506, https://doi.org/10.1080/09603409.2022.2045101.
[11] S. Sanchez, G. Gaspard, C.J. Hyde, I.A. Ashcroft, R. G.A, A.T. Clare, The creep behaviour of nickel alloy 718 manufactured by laser powder bed fusion, Mater. Des. 204 (2021) 109647, https://doi.org/10.1016/j.matdes.2021.109647.
[12] J. Nguejio, F. Szmytka, S. Hallais, A. Tanguy, S. Nardone, M. Godino Martinez, Comparison of microstructure features and mechanical properties for additive manufactured and wrought nickel alloys 625, Mater. Sci. Eng. A 764 (2019) 138214, https://doi.org/10.1016/j.msea.2019.138214.
[13] D. Monceau, M. Vilasi, High temperature oxidation of additively manufactured structural alloys, JOM 74 (2022) 1659–1667, https://doi.org/10.1007/s11837-022-05198-z.
[14] T. Galiullin, R. Pillai, W.J. Quadakkers, D. Naumenko, Differences in oxidation behavior of conventionally cast and additively manufactured Co-Base alloy MAR-M-509, High. Temp. Corros. Mater. 100 (2023) 791–816, https://doi.org/10.1007/s11085-023-10194-y.
[15] M.C. Kuner, M. Romedenne, P. Fernandez-Zelaia, S. Dryepondt, Quantitatively accounting for the effects of surface topography on the oxidation kinetics of additive manufactured Hastelloy X processed by electron beam melting, Addit. Manuf. 36 (2020) 101431, https://doi.org/10.1016/j.addma.2020.101431.
[16] M. Romedenne, R. Pillai, M. Kirka, S. Dryepondt, High temperature air oxidation behavior of Hastelloy X processed by electron beam melting (EBM) and selective laser melting (SLM), Corros. Sci. 171 (2020) 108647, https://doi.org/10.1016/j.corsci.2020.108647.
[17] M. Romedenne, P. Stack, R. Pillai, S. Dryepondt, Isothermal and cyclic oxidation of Haynes 282 processed by electron beam melting (EBM) and laser powder bed fusion (LPBF) in dry air at 800 and 950 °C, JOM 74 (2022) 1–12, https://doi.org/10.1007/s11837-022-05201-7.
[18] S. Dryepondt, M.M. Kirka, F.A. List III, Oxidation behavior of Ni-based alloys fabricated by additive manufacturing, Corros. 2019 Pap. No. C201913558 (2019) 1–13. ⟨https://www.osti.gov/servlets/purl/1658013⟩.
[19] G. de Leon Nope, G. Wang, B. Gleeson, Influence of alloy 625 manufacturing process on 950 °C oxidation behavior in air and post-oxidation high-cycle fatigue performance, High. Temp. Corros. Mater. 101 (2024) 1167–1179, https://doi.org/10.1007/s11085-024-10286-3.
[20] G. de Leon Nope, G. Wang, J.M. Alvarado-Orozco, B. Gleeson, Effects of high-temperature oxidation on fatigue life of additive-manufactured alloy 625, Miner. Met. Mater. Ser. (2023) 249–269. ⟨https://link.springer.com/chapter/10.1007/978-3-031-27447-3_17⟩ (accessed August 21, 2024).
[21] G. de Leon Nope, G. Wang, J.M. Alvarado-Orozco, B. Gleeson, Role of elemental segregation on the oxidation behavior of additively manufactured alloy 625, JOM 74 (2022) 1698–1706, https://doi.org/10.1007/s11837-022-05200-8.
[22] A. Chyrkin, K.O. Gunduz, I. Fedorova, M. Sattari, A. Visibile, M. Halvarsson, J. Froitzheim, K. Stiller, High-temperature oxidation behavior of additively manufactured IN625: effect of microstructure and grain size, Corros. Sci. 205 (2022), https://doi.org/10.1016/j.corsci.2022.110382.
[23] A. Chyrkin, W.J. Nowak, K.O. Gunduz, I. Fedorova, M. Sattari, J. Froitzheim, M. Halvarsson, K.M. Stiller, Intergranular oxidation of additively manufactured Ni-base alloy 625: the role of Si, Corros. Sci. 219 (2023) 111234, https://doi.org/10.1016/j.corsci.2023.111234.
[24] K.Y. Pineda-Arriaga, J.H. Ramírez-Ramírez, F.A. Pérez-González, J.M. Alvarado-Orozco, R. Colás, N.F. Garza-Montes-de-Oca, Characterization of the high-temperature oxidation behavior of Inconel 625® fabricated by additive manufacturing and conventional methods, Oxid. Met. 98 (2022) 489–510, https://doi.org/10.1007/s11085-022-10136-0.
[25] K.Y. Pineda-Arriaga, J.H. Ramírez-Ramírez, F.A. Pérez-González, J.M. Alvarado-Orozco, R. Colás, N.F. Garza-Montes-de-Oca, Oxidation in water vapor of Inconel 625 fabricated by additive manufacturing, High. Temp. Corros. Mater. 101 (2024) 1–11, https://doi.org/10.1007/S11085-023-10205-Y/FIGURES/8.
[26] S. Parizia, G. Marchese, M. Rashidi, M. Lorusso, E. Hryha, D. Manfredi, S. Biamino, Effect of heat treatment on microstructure and oxidation properties of Inconel 625 processed by LPBF, J. Alloy. Compd. 846 (2020) 156418, https://doi.org/10.1016/j.jallcom.2020.156418.
[27] N. Ramenatte, A. Vernouillet, S. Mathieu, A. Vande Put, M. Vilasi, D. Monceau, A comparison of the high-temperature oxidation behaviour of conventional wrought and laser beam melted Inconel 625, Corros. Sci. 164 (2020), https://doi.org/10.1016/j.corsci.2019.108347.

[28] M.R. Condruz, G. Matache, A. Paraschiv, T. Badea, V. Badilita, High temperature oxidation behavior of selective laser melting manufactured IN 625, Metals 10 (2020) 668, https://doi.org/10.3390/met10050668.

[29] E.R. Lewis, M.P. Taylor, B. Attard, N. Cruchley, A.P.C. Morrison, M.M. Attallah, S. Cruchley, Microstructural characterisation and high-temperature oxidation of laser powder bed fusion processed Inconel 625, Mater. Lett. 311 (2022) 131582, https://doi.org/10.1016/j.matlet.2021.131582.

[30] B.W. Andrade, F.E. Mariani, R.T. Coelho, A.M. de Sousa Malafaia, Comparison of the oxidation behavior at high temperature of INCONEL 625 forged and produced by additive manufacturing, High. Temp. Corros. Mater. (2024) 1–14, https://link.springer.com/article/1 0.1007/s11085-024-10283-6 (accessed August 21, 2024).

[31] M. Sharifitabar, S. Khorshahian, M. Shafiee Afarani, P. Kumar, N.K. Jain, High-temperature oxidation performance of Inconel 625 superalloy fabricated by wire arc additive manufacturing, Corros. Sci. 197 (2022) 110087, https://doi.org/10.1016/J.CORSCI.2022.110087.

[32] T. Sanviemvongsak, D. Monceau, M. Madelain, C. Desgranges, J. Smialek, B. Macquaire, Cyclic oxidation of alloy 718 produced by additive manufacturing compared to a wrought-718 alloy, Corros. Sci. 192 (2021) 109804, https://doi.org/10.1016/J.CORSCI.2021.109804.

[33] T. Sanviemvongsak, D. Monceau, C. Desgranges, B. Macquaire, Intergranular oxidation of Ni-base alloy 718 with a focus on additive manufacturing, Corros. Sci. 170 (2020) 108684, https://doi.org/10.1016/J.CORSCI.2020.108684.

[34] T. Sanviemvongsak, D. Monceau, B. Macquaire, High temperature oxidation of IN 718 manufactured by laser beam melting and electron beam melting: effect of surface topography, Corros. Sci. 141 (2018) 127–145, https://doi.org/10.1016/J.CORSCI.2018.07.005.

[35] H. Yu, S. Hayashi, K. Kakehi, Y.L. Kuo, Study of formed oxides in IN718 alloy during the fabrication by selective laser melting and electron beam melting, Metals 9 (2018) 19, https://doi.org/10.3390/MET9010019.

[36] C. Juillet, A. Oudriss, J. Balmain, X. Feaugas, F. Pedraza, Characterization and oxidation resistance of additive manufactured and forged IN718 Ni-based superalloys, Corros. Sci. 142 (2018) 266–276, https://doi.org/10.1016/j.corsci.2018.07.032.

[37] M. Calandri, D. Manfredi, F. Calignano, E.P. Ambrosio, S. Biamino, R. Lupoi, D. Ugues, Solution treatment study of Inconel 718 produced by SLM additive technique in view of the oxidation resistance, Adv. Eng. Mater. 20 (2018) 1800351, https://doi.org/10.1002/adem.201800351.

[38] A. Chyrkin, P. Huczkowski, V. Shemet, L. Singheiser, W.J. Quadakkers, Sub-scale depletion and enrichment processes during high temperature oxidation of the nickel base alloy 625 in the temperature range 900-1000 °c, Oxid. Met. 75 (2011), https://doi.org/10.1007/s11085-010-9225-3.

[39] D.L. Douglass, J.S. Armijo, The effect of silicon and manganese on the oxidation mechanism of Ni-20 Cr, Oxid. Met. 2 (1970) 207–231, https://doi.org/10.1007/BF00603657.

[40] H.E. Evans, D.A. Hilton, R.A. Holm, S.J. Webster, Influence of silicon additions on the oxidation resistance of a stainless steel, Oxid. Met. 19 (1983) 1–18, https://doi.org/10.1007/BF00656225.

[41] R.C. Lobb, J.A. Sasse, H.E. Evans, Dependence of oxidation behaviour on silicon content of 20%Cr austenitic steels, Mater. Sci. Technol. 5 (1989) 828–834, https://doi.org/10.1179/mst.1989.5.8.828.

[42] B. Li, B. Gleeson, Effects of silicon on the oxidation behavior of Ni-base chromia-forming alloys, Oxid. Met. 65 (2006) 101–122, https://doi.org/10.1007/s11085-006-9003-4.

[43] W.J. Quadakkers, D. Naumenko, L. Singheiser, H.J. Penkalla, A.K. Tyagi, A. Czyrska-Filemonowicz, Batch to batch variations in the oxidation behaviour of alumina forming Fe-based alloys, Mater. Corros. 51 (2000) 350–357, https://doi.org/10.1002/(SICI)1521-4176(200005)51:5<350::AID-MACO350>3.0.CO;2-7.

[44] A. Kreitcberg, V. Brailovski, S. Turenne, Effect of heat treatment and hot isostatic pressing on the microstructure and mechanical properties of Inconel 625 alloy processed by laser powder bed fusion, Materials Science Engineering A 689 (2017) 1–10, https://doi.org/10.1016/j.msea.2017.02.038.

[45] A. Naoumidis, H.A. Schulze, W. Jungen, P. Lersch, Phase studies in the chromium-manganese-titanium oxide system at different oxygen partial pressures, J. Eur. Ceram. Soc. 7 (1991) 55–63, https://doi.org/10.1016/0955-2219(91)90054-4.

[46] A. Chyrkin, A. Fazi, M. Sattari, D. Mayweg, M. Thuvander, K. Stiller, M. Halvarsson, W.J. Nowak, E. Wessel, D. Naumenko, J. Froitzheim, Oxidation of additively manufactured Ni-base alloy IN625: Mechanism of intergranular oxidation, Corros. Sci. 256 (2025) 113218, https://doi.org/10.1016/j.corsci.2025.113218.

[47] X. Guo, H.L. Huang, M. Zhu, K. Hariharan, S.C. Chien, N. Huynh, J. Hwang, W. Windl, C.D. Taylor, E.J. Schindelholz, G.S. Frankel, Interstitial elements created via metal 3D printing, Mater. Today 66 (2023) 92–104, https://doi.org/10.1016/J.MATTOD.2023.04.020.

[48] N. Choi, M. da Silva Pinto, S. Yang, J.H. Yu, J.S. Lee, M. Luckabauer, G. Wilde, S. V. Divinski, Grain boundary diffusion in additively manufactured CoCrFeMnNi high-entropy alloys: Impact of non-equilibrium state, temperature and relaxation, Mater. (Oxf.) 38 (2024) 102228, https://doi.org/10.1016/J.MTLA.2024.102228.

[49] C. Wagner, Oxidation of alloys involving noble metals, J. Electrochem Soc. 103 (1956) 571, https://doi.org/10.1149/1.2430159.

[50] G.B. Gibbs, A model for mild steel oxidation in CO2, Oxid. Met. 7 (1973) 173–184, https://doi.org/10.1007/BF00610578/METRICS.

[51] R.P. Oleksak, M. Kapoor, D.E. Perea, G.R. Holcomb, Ö.N. Doğan, The role of metal vacancies during high-temperature oxidation of alloys, Npj Mater. Degrad. 2018 21 2 (2018) 1–8, https://doi.org/10.1038/s41529-018-0046-1.

[52] A. Chyrkin, A. Fazi, M. Sattari, M. Thuvander, K. Stiller, M. Halvarsson, E. Wessel, D. Naumenko, J. Froitzheim, PVD Ce-coating to mitigate intergranular oxidation of additively manufactured Ni-base alloy IN625, Npj Mater. Degrad. 2025 91 9 (2025) 1–13, https://doi.org/10.1038/s41529-025-00677-5.

[53] A. Galerie, F. Toscan, E. N'Dah, K. Przybylski, Y. Wouters, M. Dupeux, Measuring adhesion of C2O3 and Al2O3 scales on Fe-based alloys, Mater. Sci. Forum 461–464 (2004) 631–638, https://doi.org/10.4028/www.scientific.net/MSF.461-464.631.

[54] A. Galerie, F. Toscan, M. Dupeux, J. Mougin, G. Lucazeau, C. Valot, A.-M. Huntz, L. Antoni, Stress and adhesion of chromia-rich scales on ferritic stainless steels in relation with spallation, Mater. Res. 7 (2004) 81–88, https://doi.org/10.1590/S1516-14392004000100012.

[55] J. Mougin, M. Dupeux, L. Antoni, A.A. Galerie, Adhesion of thermal oxide scales grown on ferritic stainless steels measured using the inverted blister test, Materials Science Engineering A 359 (2003) 44–51, https://doi.org/10.1016/S0921-5093(03)00355-1.

[56] G. Bamba, Y. Wouters, A. Galerie, F. Charlot, A. Dellali, Thermal oxidation kinetics and oxide scale adhesion of Fe–15Cr alloys as a function of their silicon content, Acta Mater. 54 (2006) 3917–3922, https://doi.org/10.1016/j.actamat.2006.04.023.

[57] D.P. Whittle, J. Stringer, Improvements in high temperature oxidation resistance by additions of reactive elements or oxide dispersions, Philos. Trans. R. Soc. Lond. Ser. A Math. Phys. Sci. 295 (1980) 309–329, https://doi.org/10.1098/RSTA.1980.0124.

[58] P.Y. Hou, The reactive element effect – Past, present and future, Mater. Sci. Forum 696 (2011) 39–44, https://doi.org/10.4028/WWW.SCIENTIFIC.NET/MSF.696.39.

[59] B.A. Pint, Progress in understanding the reactive element effect since the Whittle and Stringer literature review, John String Symp High. Temp. Corros. (2001) 9–19.

[60] D. Naumenko, B.A. Pint, W.J. Quadakkers, Current thoughts on reactive element effects in alumina-forming systems: In memory of John Stringer, Oxid. Met. 2016 861 86 (2016) 1–43, https://doi.org/10.1007/S11085-016-9625-0.

[61] P.Y. Hou, J. Stringer, The effect of aluminum as an alloying addition or as an implant on the high-temperature oxidation of Ni-25Cr, Oxid. Met. 34 (1990) 299–321, https://doi.org/10.1007/BF00665020/METRICS.

[62] P.Y. Hou, J. Stringer, The effect of reactive element additions on the selective oxidation, growth and adhesion of chromia scales, Materials Science Engineering A 202 (1995) 1–10, https://doi.org/10.1016/0921-5093(95)09798-8.

[63] F.H. Stott, F.I. Wei, C.A. Enahoro, The influence of manganese on the High-temperature oxidation of iron-chromium alloys, Mater. Corros. 40 (1989) 198–205, https://doi.org/10.1002/MACO.19890400403.

[64] A.L. Marasco, D.J. Young, The oxidation of Iron-Chromium-Manganese alloys at 900°C, Oxid. Met. 36 (1991) 157–174, https://doi.org/10.1007/BF00938460/METRICS.

[65] G.R. Holcomb, D.E. Alman, The effect of manganese additions on the reactive evaporation of chromium in Ni–Cr alloys, Scr. Mater. 54 (2006) 1821–1825, https://doi.org/10.1016/j.scriptamat.2006.01.026.

[66] V. Miguel-Pérez, A. Martínez-Amesti, M.L. Nó, A. Larrañaga, M.I. Arriortua, Oxide scale formation on different metallic interconnects for solid oxide fuel cells, Corros. Sci. 60 (2012) 38–49, https://doi.org/10.1016/j.corsci.2012.04.014.

[67] D.W. Yun, S.M. Seo, H.W. Jeong, Y.S. Yoo, The effects of the minor alloying elements Al, Si and Mn on the cyclic oxidation of Ni–Cr–W–Mo alloys, Corros. Sci. 83 (2014) 176–188, https://doi.org/10.1016/j.corsci.2014.02.015.

[68] F.H. Stott, F.I. Wei, Comparison of the effects of small additions of silicon or aluminum on the oxidation of iron-chromium alloys, Oxid. Met. 31 (1989) 369–391, https://doi.org/10.1007/BF00666463.

[69] B. Ahmad, P. Fox, STEM analysis of the transient oxidation of a Ni-20Cr alloy at high temperature, Oxid. Met. 52 (1999) 113–138, https://doi.org/10.1023/A:1018827108376/METRICS.

[70] J.E. Truman, K.R. Pirt, The influence of the content of certain incidental elements on the cyclic oxidation resistance of 12–13% chromium steels, Corros. Sci. 16 (1976) 103–108, https://doi.org/10.1016/0010-938X(76)90035-4.

[71] F.H. Stott, G.J. Gabriel, G.C. Wood, The influence of silicon on the high-temperature oxidation of nickel, Oxid. Met. 28 (1987) 329–345, https://doi.org/10.1007/BF00666726.

[72] B. Ahmad, P. Fox, STEM analysis of the transient oxidation of a Ni-20Cr alloy at high temperature, Oxid. Met. 52 (1999) 113–138, https://doi.org/10.1023/A:1018827108376.

[73] A. Vayyala, I. Povstugar, D. Naumenko, W.J. Quadakkers, H. Hattendorf, J. Mayer, A nanoscale study of thermally grown chromia on high-Cr ferritic steels and associated oxidation mechanisms, J. Electrochem Soc. 167 (2020) 061502, https://doi.org/10.1149/1945-7111/AB7D2E.

[74] C. Siri, I. Popa, A. Vion, C. Langlade, S. Chevalier, Impact of selective laser melting additive manufacturing on the high temperature behavior of AISI 316L austenitic stainless steel, Oxid. Met. 94 (2020) 527–548, https://doi.org/10.1007/S11085-020-10005-8/FIGURES/11.

[75] C. Siri, I. Popa, A. Vion, C. Langlade, S. Chevalier, Impact of water vapor on the high temperature oxidation of wrought and Selective Laser Melted (SLM) AISI 316L, Oxid. Met. 96 (2021) 347–359, https://doi.org/10.1007/S11085-021-10062-7/TABLES/1.

[76] R. Hu, X. Liu, Z. Hang, K. Zhang, B. Jiang, X. Luo, Laser additive manufacturing of a TiN strengthened nickel-based superalloy with tailored microstructure and tensile performance, Mater. Sci. Eng. A 940 (2025) 148569, https://doi.org/10.1016/J.MSEA.2025.148569.

[77] T. Gheno, C. Rio, E. Rimpot, S. Mercier, Kinetics of alloy depletion during selective oxidation in polycrystals, High. Temp. Corros. Mater. 100 (2023) 709–743, https://doi.org/10.1007/S11085-023-10187-X/FIGURES/23.

[78] G. Wang, H. Ouyang, C. Fan, Q. Guo, Z. Li, W. Yan, Z. Li, The origin of high-density dislocations in additively manufactured metals, Mater. Res Lett. 8 (2020) 283–290, https://doi.org/10.1080/21663831.2020.1751739.

[79] D. Hu, N. Grilli, W. Yan, Dislocation structures formation induced by thermal stress in additive manufacturing: multiscale crystal plasticity modeling of dislocation transport, J. Mech. Phys. Solids 173 (2023) 105235, https://doi.org/10.1016/J.JMPS.2023.105235.
[80] Z. Li, Y. Cui, W. Yan, D. Zhang, Y. Fang, Y. Chen, Q. Yu, G. Wang, H. Ouyang, C. Fan, Q. Guo, D.B. Xiong, S. Jin, G. Sha, N. Ghoniem, Z. Zhang, Y.M. Wang, Enhanced strengthening and hardening via self-stabilized dislocation network in additively manufactured metals, Mater. Today 50 (2021) 79–88, https://doi.org/10.1016/J.MATTOD.2021.06.002.
[81] S. Gao, Z. Li, S. Van Petegem, J. Ge, S. Goel, J.V. Vas, V. Luzin, Z. Hu, H.L. Seet, D. F. Sanchez, H. Van Swygenhoven, H. Gao, M. Seita, Additive manufacturing of alloys with programmable microstructure and properties, Nat. Commun. 2023 141 14 (2023) 1–11, https://doi.org/10.1038/s41467-023-42326-y.
[82] G.R. Love, Dislocation pipe diffusion, Acta Metall. 12 (1964) 731–737, https://doi.org/10.1016/0001-6160(64)90220-2.
[83] J. Mimkes, Pipe diffusion along isolated dislocations, Thin Solid Films 25 (1975) 221–230, https://doi.org/10.1016/0040-6090(75)90258-8.
[84] A. Chyrkin, S.L. Schulze, J. Pirón-Abellán, W. Bleck, L. Singheiser, W. J. Quadakkers, Oxidation limited lifetime of Ni-base metal foams in the temperature range 700-900°C, Adv. Eng. Mater. 12 (2010), https://doi.org/10.1002/adem.201000139.
[85] A. Chyrkin, J. Froitzheim, Premature breakaway oxidation of ferritic stainless steels triggered by austenitization, Corros. Sci. 256 (2025) 113260, https://doi.org/10.1016/J.CORSCI.2025.113260.
[86] S. Leistikow, I. Wolf, H.J. Grabke, Effect of cold work on the oxidation behavior and carburization resistance of Alloy 800, Werkst. Und Korros. 38 (1987) 556–562.
[87] C. Sundaresan, B. Ghule, H.C. Dey, S. Ningshen, D. Vijayshankar, V.S. Raja, Oxidation behaviour of austenitic stainless steel 304HCu in advanced ultra supercritical (AUSC) steam and the efficacy of shot-peening treatment, Corros. Sci. 235 (2024) 112214, https://doi.org/10.1016/J.CORSCI.2024.112214.
[88] L. Tan, X. Ren, K. Sridharan, T.R. Allen, Effect of shot-peening on the oxidation of alloy 800H exposed to supercritical water and cyclic oxidation, Corros. Sci. 50 (2008) 2040–2046, https://doi.org/10.1016/J.CORSCI.2008.04.008.
[89] J. Kundin, A. Riyahi khorasgani, R. Schiedung, B. Camin, I. Steinbach, Modeling vacancy-induced porosity in compositionally-graded complex alloys, Acta Mater. 271 (2024) 119905, https://doi.org/10.1016/J.ACTAMAT.2024.119905.
[90] A. Riyahi khorasgani, I. Steinbach, B. Camin, J. Kundin, A phase-field study to explore the nature of the morphological instability of Kirkendall voids in complex alloys, Sci. Rep. 2024 141 14 (2024) 1–17, https://doi.org/10.1038/s41598-024-81532-6.
[91] C. Desgranges, F. Lequien, E. Aublant, M. Nastar, D. Monceau, Depletion and voids formation in the substrate during high temperature oxidation of Ni-Cr alloys, Oxid. Met. 79 (2013) 93–105, https://doi.org/10.1007/S11085-012-9328-0/FIGURES/6.